Laercio Meneses Silva Junior

STRESS ANALYSIS ON A THIN-WALLED COMPOSITE BLADE OF A LARGE WIND TURBINE

Dissertation submitted to the Mechanical Engineering Graduate Program of the Federal University of Santa Catarina for the obtention of the degree of Master of Science in Mechanical Engineering.

Advisor: Prof. Edison da Rosa, Dr. Eng.

Co-Advisor: Prof. José Carlos de Carvalho Pereira, Dr. Eng.

Florianópolis

2016

Ficha de identificação da obra elaborada pelo autor,
através do Programa de Geração Automática da Biblioteca Universitária da UFSC.

Silva Junior, Laercio Meneses
Stress Analysis On A Thin-Walled Composite Blade Of A Large Wind Turbine / Laercio Meneses Silva Junior ; orientador, Edison Da Rosa ; coorientador, José Carlos de Carvalho Pereira. - Florianópolis, SC, 2016.
116 p.

Dissertação (mestrado) - Universidade Federal de Santa Catarina, Centro Tecnológico. Programa de Pós-Graduação em Engenharia Mecânica.

Inclui referências

1. Engenharia Mecânica. 2. Large wind turbine. 3. Specific power. 4. Reynolds. 5. Composites. I. Da Rosa, Edison. II. Pereira, José Carlos de Carvalho. III. Universidade Federal de Santa Catarina. Programa de Pós Graduação em Engenharia Mecânica. IV. Título.

Laercio Meneses Silva Junior

STRESS ANALYSIS ON A THIN-WALLED COMPOSITE BLADE OF A LARGE WIND TURBINE

This dissertation was judged suitable for obtaining the title of "Master in Mechanical Engineering" and approved in its final form by the Graduate Program in Mechanical Engineering.

Florianópolis, September 29th, 2016.

_____

Prof. Dr. Jonny Carlos da Silva – Coordinator
Federal University of Santa Catarina

_____

Prof. Dr. Edison da Rosa – Advisor
Federal University of Santa Catarina

_____

Prof. Dr. José Carlos de Carvalho Pereira – Co-Advisor
Federal University of Santa Catarina

Examination Board:

_____

Prof. Dr. Júlio César Passos
Federal University of Santa Catarina

_____

Prof. Dr. Marcelo Krajnc Alves
Federal University of Santa Catarina

Prof. Dr. Clóvis Sperb De Barcellos
Federal University of Santa Catarina

Prof. Dr. Otávio Augusto Alves da Silveira
Federal University of Santa Catarina

ACKNOWLEDGMENTS

I express my sincere gratitude to the professors of the Department of Mechanical Engineering of the Federal University of Santa Catarina, especially to my co-advisor Prof. José Carlos de Carvalho Pereira, for all his guidance, support and encouragement throughout my graduate studies.

I also thank the colleagues of Grante and my family for the good times, conversations, support and encouragement during this important period of my life.

“Ideas and only ideas can light the darkness”

Ludwig Von Mises

ABSTRACT

Research institutes and industry have recently initiated the development of wind turbines for energy production at sites with lower wind speeds. The relatively high electric power production of this type of wind turbine is related to the growing of the swept area. Thus, in order to increase the swept area, the length of the new blades must be greater than the ones of traditional blades for horizontal axis wind turbines. The expansion of the rotors diameter of large wind turbines has some implications, such as the increase of gravity loads and new transportation logistics challenges. To overcome these challenges, advances in the blade technology have led to more efficient structural and aerodynamic design and optimized material usage. In this context, analytical models have to accurately predict aerodynamic loads acting on the blades and calculate the structural stresses developed during the turbine operation. Since composite materials have high strength/weight ratio compared to other structural materials and are flexible with respect to the fabrication process, they are more appropriate for blade applications. This dissertation presents an improvement in the aerodynamic model that takes into account an iterative procedure for determining Reynolds number instead of depending on experimental data for the process of airfoil selection along the blade span that maximize the power extracted from the wind. The multilayer shell theories and the relationship between the aerodynamic bending and torsional moments acting on the blade are presented. The in-plane normal and shear stresses on the thin-walled multilayer blade are determined by using the Shear Flow Theory. A case study is conducted on a 20 MW wind turbine developed in the Energy Research Centre of the Netherlands-ECN. The normal and shear stresses are calculated and the Tsai-Wu criterion is applied for the strength evaluation of the blade made of glass/epoxy. Results obtained with two stacking sequences are presented.

Keywords: *Large wind turbine, specific power, Reynolds, composites, Tsai-Wu.*

RESUMO

Institutos de pesquisa e a indústria iniciaram recentemente o desenvolvimento de turbinas eólicas para a produção de energia em locais com baixas velocidades de vento. A produção de energia elétrica relativamente alta deste tipo de turbina está relacionada com o crescimento da área varrida pelo rotor. Assim, de forma a aumentar a área varrida, o comprimento das novas pás deve ser maior que o das pás tradicionais de turbinas eólicas de eixo horizontal. O aumento do diâmetro dos rotores das turbinas eólicas tem algumas implicações, tais como o aumento das cargas gravitacionais e desafios no seu transporte. Para superá-los, avanços na tecnologia de pás têm levado a projetos estruturais e aerodinâmicos mais eficientes. Neste contexto, modelos analíticos têm de prever com precisão as cargas aerodinâmicas atuando sobre as pás, além de calcular as tensões estruturais desenvolvidas durante sua operação. Uma vez que materiais compostos têm uma elevada relação resistência/peso em comparação com outros materiais estruturais, além de serem flexíveis no que diz respeito ao processo de fabricação, estes materiais têm sido os mais investigados para aplicações em pás de turbina eólica. Esta dissertação apresenta uma melhoria no modelo aerodinâmico que leva em conta um processo iterativo para a determinação do número de Reynolds, em vez de depender de dados experimentais para o processo de escolha do aerofólio ao longo da envergadura da pá que maximiza a potência extraída do vento. As teorias de cascas multilaminares e a relação entre os momentos aerodinâmicos fletores e de torção que atuam sobre a pá são apresentados. As tensões normais e de cisalhamento atuantes no plano da pá multilaminar de parede fina são determinadas utilizando a Teoria do Fluxo de Cisalhamento. Um estudo de caso é conduzido em uma turbina eólica de 20 MW desenvolvida no Centro de Pesquisa em Energia dos Países Baixos (ECN). As tensões normais e de cisalhamento são calculadas e o critério de Tsai-Wu é aplicado para a avaliação da resistência da pá feita em vidro/epóxi. Os resultados obtidos com duas sequências de empilhamento de lâminas são apresentados.

Palavras-chave: *Turbina eólica de grande porte, potência específica, Reynolds, compósitos, Tsai-Wu*

TABLE OF CONTENTS

Page

LIST OF FIGURES

Figure Page

LIST OF TABLES

Table Page

LIST OF SYMBOLS

P_{wind}	[W]	Power available in the wind
ρ	[kg/m^3]	Ambient air density
A	[m^2]	Area swept by the rotor
U	[m/s]	Wind speed
σ	[Pa]	Normal stress
E	[Pa]	Young Modulus
G	[Pa]	Shear Modulus
ε	-	Normal strain
$\dot{\varepsilon}$	[s^{-1}]	Normal strain rate
T	[N]	Thrust force
Q	[Nm]	Torque
$\dot{m}$	[kg/s]	Mass flow rate
p	[N/m^2]	Pressure
a	-	Axial induction factor – fractional decrease in wind velocity between the free stream and the stream at the rotor plane
a'	-	Angular induction factor
C_P	-	Power coefficient
C_T	-	Thrust coefficient
ω	[rad/s]	Rotational velocity of the airflow behind the rotor
Ω	[rad/s]	Rotational velocity of the blade
r	[m]	Radial distance from the rotation axis
R	[m]	Total length of the blade
λ	-	Tip speed ratio

μ	-	Fraction of the radius R
c	[m]	Chord – distance between the leading edge and the trailing edge
β	[º]	Pitch angle (between the chord and the rotation plane)
v_a	[m/s]	Induced axial velocity
v_t	[m/s]	Induced tangential velocity
W	[m/s]	Resulting velocity of the incident flow
α	[º]	Angle of attack (between the incoming airflow W and the chord c)
ϕ	[º]	Angle between the turbine rotation plane and the resulting wind direction
L	[N]	Lift force
D	[N]	Drag force
M	[Nm]	Pitching moment
C_l	-	Lift coefficient
C_d	-	Drag coefficient
C_m	-	Pitching moment coefficient
Re	-	Reynolds number
ν	[m²/s]	Kinematic viscosity of the air
B	-	Number of turbine blades
σ_r	-	Blade solidity parameter – ratio between the total area of the elements in r and the area of the ring swept by them
F_{tip}	-	Correction factor for the tip losses
F_c	-	Correction factor for the root losses
Ϙ	-	Turbine total efficiency

$\varepsilon_{1,2,3}$	-	Normal strain in the orthotropic axis
$\gamma_{1,2,3}$	-	Shear strain in the orthotropic axis
$\sigma_{1,2,3}$	[Pa]	Normal stress in the orthotropic axis
$\tau_{1,2,3}$	[Pa]	Shear stress in the orthotropic axis
ν_{12}, ν_{21}	-	Major and minor Poisson's ratio
$\varepsilon_{x,y}$	-	Normal strain in the local axis
τ_{xy}	-	Shear strain in the local axis
$\sigma_{x,y}$	[Pa]	Normal stress in the local axis
τ_{xy}	[Pa]	Shear stress in the local axis
h_k	[m]	Thickness of the layer k
θ_k	[º]	Fiber direction of the layer k with respect to direction x of the local axis
$\varepsilon_x^0, \varepsilon_y^0$	-	Normal strains in the neutral surface
γ_{xy}^0	-	Shear strain in the neutral surface
κ	-	Curvature
M_t, M_a	[Nm]	Bending moments
M_r	[Nm]	Torsional moment
Q_t, Q_a	[N]	Shear forces
EI_x	[Pa]	Flapwise stiffness
EI_y	[Pa]	Edgewise stiffness
GJ	[Pa]	Torsional stifness

CHAPTER 1

INTRODUCTION

This chapter provides an introduction in large wind turbine blade technology conducted for this study. First, a brief introduction to the wind energy production, the world and the brazilian scenario and the wind energy capacity improvements are discussed. Then the motivation for the research conducted in this dissertation is presented. The chapter ends with the objectives for the present study, followed by an outline of the subsequent chapters of this dissertation.

1.1 Introduction to the Wind Energy Production

A wind turbine is a mechanical device that converts the kinetic energy available in the wind into rotational energy of its rotor and subsequently into electrical energy of its generator. The horizontal axis wind turbine (HAWT), object of this study, historically uses a three-bladed rotor to extract energy from the wind. The net kinetic energy available in the wind for conversion is the one that flows through the area swept by the rotor. Thus, the power available in the wind is this kinetic energy per unit time expressed as

$$P_{wind} = \frac{1}{2}\rho A U^3 \tag{1.1}$$

where ρ is the ambient air density at the site, A is the area swept by the rotor and U is the wind speed [1], which is assumed uniform across the rotor disc. Based on this equation, it can be observed that the power potentially extractable by the turbine is proportional to the swept area of the rotor and to the cube of the wind speed. Obviously, the best sites for wind plant installation are the ones where the wind speeds are the highest.

As a natural resource dispersed in the environment, the wind speed is variable and depends on the height of the turbine hub (axis of the rotor)

above the ground, on the geographic location of the wind plant (because of global wind patterns), the season of the year and the time of the day [2]. As illustrated in Figure 1.1, the higher is the hub, the higher is the wind speed in the lowest layer of air near the Earth's surface [3]. This implies that by increasing the hub height, the rotor can capture more energy for the same swept area. The wind speed is also influenced by the intensity of solar heating, local terrain conditions, presence of vegetation, man-made obstacles and latitude [2]. The variability in the wind profile over short periods of time along the day is due to the turbulence intensity. This fact has two implications: the variability of the power output of the wind turbine and structural loads fluctuation that can impact the wind turbine reliability.

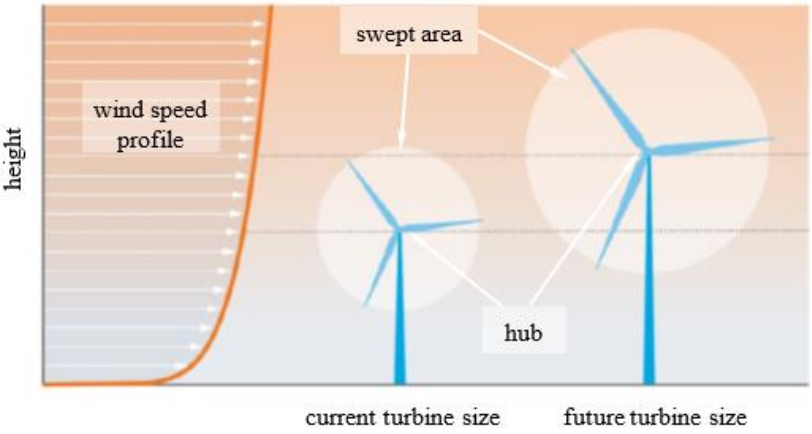

Figure 1.1 – Representative wind atmospheric boundary layer velocity profile with two turbines of different heights. (Source: NREL [3])

On regional scale, the wind speed at a given height above the ground is mainly affected by topography and vegetation that affect the wind flow. As it can be observed on the United States Wind Atlas illustrated in Figure 1.2 and on the Brazilian Wind Atlas illustrated in Figure 1.3, the best sites for wind energy production are preferably in the west and east coast and in the midwest for the United States, and in the northeast and south coast for Brazil, respectively. Since these land areas are small compared to the

total area of the country, for increasing the wind energy production capacity, the exploration of other regions with lower wind speeds is also important.

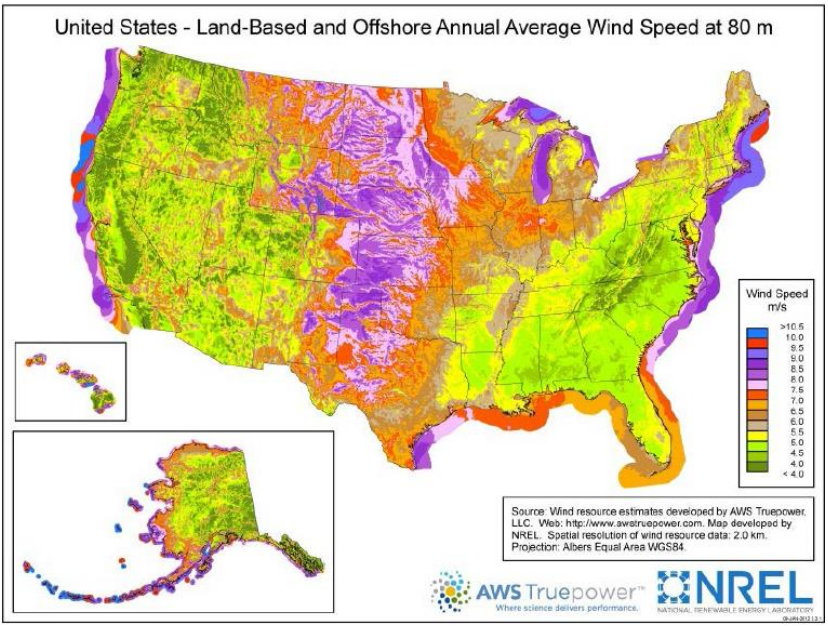

Figure 1.2 – U.S. Wind Atlas (average wind speed at 80 m). (Source: NREL [3])

Another way to increase the energy captured from the wind is to enlarge the swept area. Hence, the dominant trend of wind power production over the years has been the growth in rotor size and the reduction of energy costs. Advances in the blade design technology have been achieved through more efficient structural and aerodynamic design and optimized material usage [4].

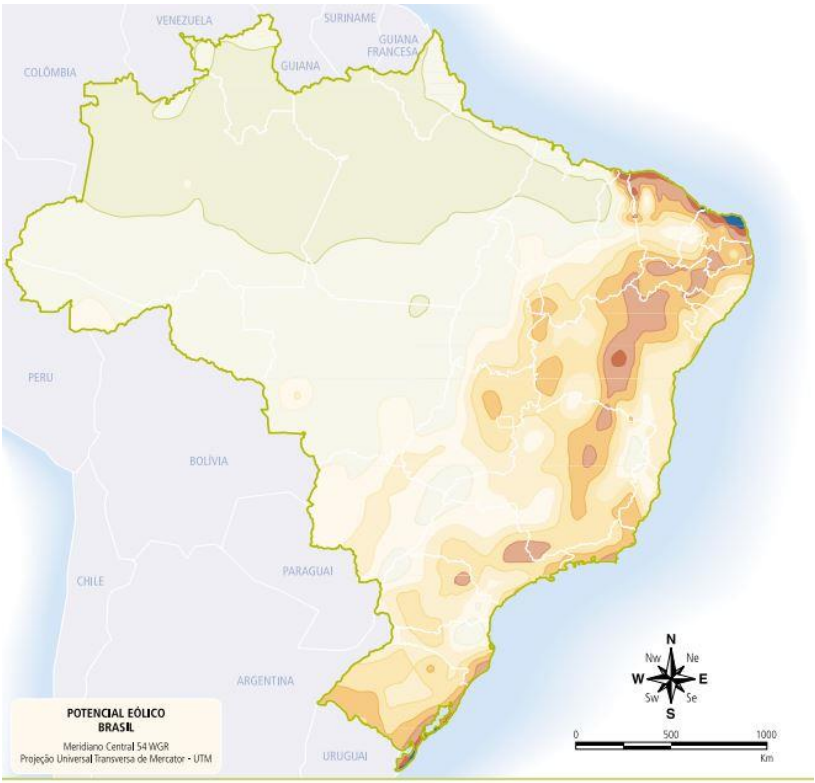

Velocidade média do vento (m/s)
50 m acima do nível da superfície

Classes de energia	Mata	Campo Aberto	Zona Costeira	Morro	Montanha
4	> 6,0	> 7,0	> 8,0	> 9,0	> 11,0
3	4,5 - 6,0	6,0 - 7,0	6,0 - 7,0	7,5 - 9,0	8,5 - 11,0
2	3,0 - 4,5	4,5 - 6,0	4,5 - 6,0	6,0 - 7,5	7,0 - 8,5
1	< 3,0	< 4,5	< 4,5	< 6,0	< 7,0

NOTAS:

Mata indica áreas de vegetação nativa, com arbustos e árvores altas.

Campo aberto refere-se a áreas planas de pastagens, plantações e/ ou vegetação baixa, sem muitas árvores altas.

Zonas costeiras são áreas de praia, normalmente com larga faixa de areia, onde o vento incide predominantemente no sentido mar-terra.

Morros são áreas de relevo levemente ondulado, relativamente complexo e de pouca vegetação ou pasto.

Montanhas representam áreas de relevo complexo com altas montanhas. O potencial eólico é dado para locais nos topos das montanhas em condições favoráveis para o fluxo de vento.

Figure 1.3 – Brazilian Wind Atlas (annual average speed at 50 m). (Source: ANEEL [5])

Due to the variable nature of wind, the power output of a wind turbine varies with time. So, when evaluating the economics of wind turbines, it is often useful to look at the annual energy production (AEP). AEP is the net energy produced by the turbine or a plant over the course of one year. Estimating AEP requires knowledge of the power curve of the turbine and

statistical approximation of the site specific availability of wind at heights of interest [3].

In Figure 1.4, the wind power curve (grey) indicates the power potential of the wind itself. The wind turbine power curve (orange) indicates the power generated by the turbine as a function of the wind speed. The Weibull curve (blue) provides statistical estimates of the fractional time in a given year when the wind speed is a given value for a specific site. Together, the wind turbine power curve and the Weibull distribution estimate the contribution to the AEP at each wind speed, as shown by the green curve. The area under the green curve is the net AEP [3].

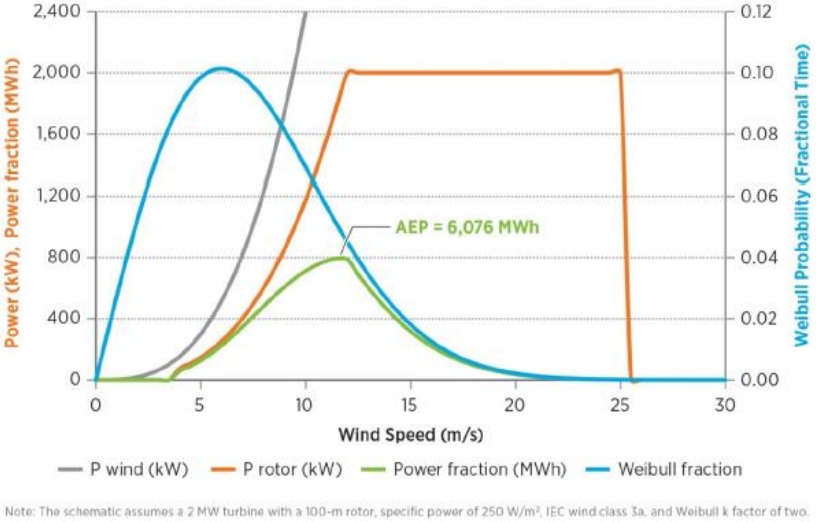

Figure 1.4 – Schematic relationship among wind speed, the wind speed distribution (Weibull), a typical wind turbine power curve and the amount of energy produced by the turbine given the wind speed distribution. (Source: NREL [3])

Another quantity used to compare wind power plants with conventional fossil power plants is the capacity factor. The capacity factor (CF), a measure of efficiency of the power plant, is defined as

$$CF = \frac{AEP}{Rated\ Power \times 24 \times 365} \tag{1.2}$$

Because of the variability of the wind, at speeds below the rated wind speed, the turbine produces less than the rated power. Figure 1.5 shows a typical power curve for a modern wind turbine. The turbine requires a minimum wind speed, called cut-in wind speed, before it is able to extract power from the wind. This speed is usually based on generator design limits. At speeds above the cut-in wind speed, power generation increases as the cube of the wind speed until the rotor hits the rated power. Finally, at higher wind speeds, machines have a cut-out wind speed, where the turbine shuts down to prevent mechanical damage from excessive loads on the turbine components [3].

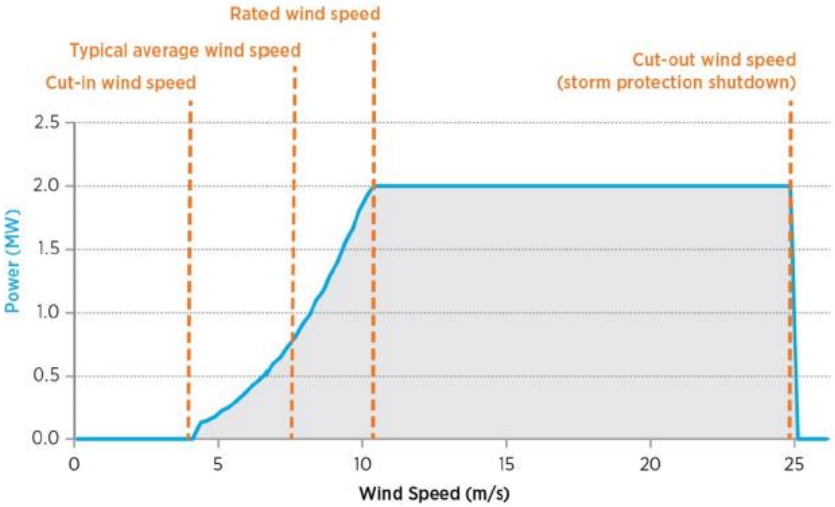

Figure 1.5 – Typical power curve for a modern wind turbine. (Source: NREL [3])

Increasing wind plant capacity factor through technology innovation is critical to make wind energy economic and competitive with conventional energy sources. Turbine equipment manufacturers have focused on increasing capacity factor by reducing rotor specific power aiming to

make turbines cost effective at low wind speed sites. By lowering the rotor specific power, i.e., increasing rotor diameter for the same turbine power rating, the machine generates more power at lower wind speeds [3]. This shifts the power curve to the left and increases the capacity factor, as shown by Figure 1.6.

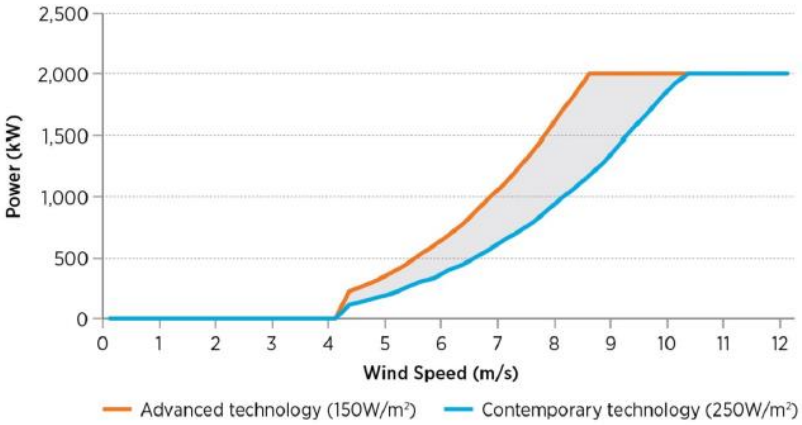

Figure 1.6 – Power curve shift in the region between cut-in speed and rated wind speed resulting from use of rotors with lower specific power. (Source: NREL [3]).

This increase in capacity factor is often more than sufficient to offset the increased capital costs of a larger rotor and makes wind power economical in low wind speed sites [3].

Despite the trends over the past decade in the average hub height, rotor diameter and nameplate capacity of turbines have been to increase, the growth of the rotor diameter has been particularly rapid. With growth in the average swept area (m²) outpacing growth in average nameplate capacity (W), there has been a decline in the average specific power (W/m²) among the U.S. turbine fleet, from around 400 W/m² among projects installed in 1998–1999 to 255 W/m² among projects installed in 2013 (Figure 1.7). The decline in specific power was especially rapid from 2001 to 2004 and, more recently, from 2011 to 2013. Though a slow

year for wind installations overall, 2013 saw a significant jump in market share for turbines with a specific power of less than 220 W/m² [6].

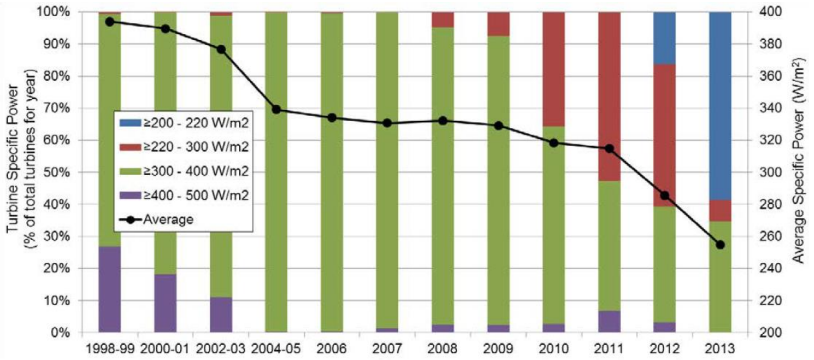

Figure 1.7 – Trends in wind turbines specific power. (Source: U.S. Department of Energy [6])

Innovations underway today could allow wind turbines to achieve even lower specific power as a result of continued growth in rotor size relative to nameplate capacity, as it can be observed in Figure 1.8.

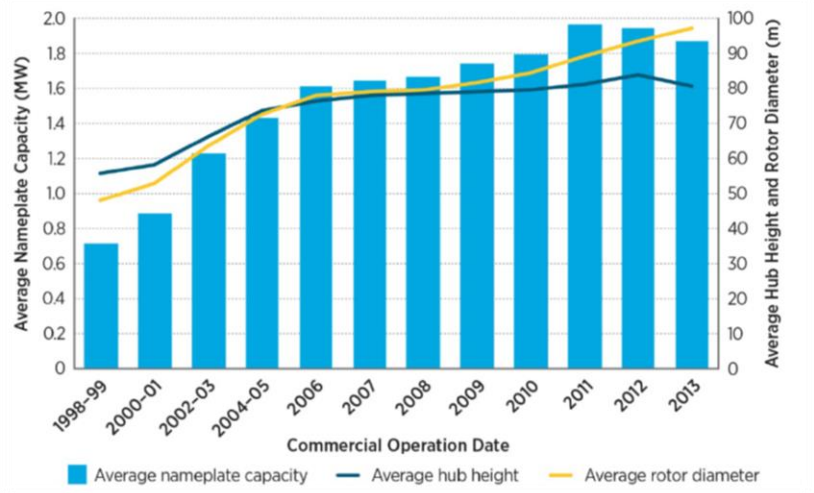

Figure 1.8 – Average turbine nameplate capacity, rotor diameter and hub height installed during the period 1998-2013. (Source: U.S. Department of Energy [6])

In early 2014, Vestas claimed the title of holder of the largest wind turbine in the world, with the installation of the V164-8MW prototype in the Danish National Tests Centre for Large Wind Turbines, in Østerild [7].

The fate of the turbine is to be the flag ship of the joint venture announced between Vestas and Mitsubishi Heavy Industries (MHI), which will combine their technologies and experience and probably make inroads into the incipient offshore wind energy market in Japan [7].

Vestas says the new 8 MW turbine, scheduled to go into mass production in 2015, will generate 30% more power than the current holder of this record [7]. The V164-8MW, Figure 1.9, has a diameter of 164 meters, tower height of 140 meters and blades of 80 meters.

Figure 1.9 – Vestas V164-8MW. (Source: Wind Power Monthly [8])

The title of the largest offshore wind turbine in the world belonged, previously, to the S7.0-171-7MW (Figure 1.10 (a), by Samsung Heavy Industries, which is being installed in the sea, in Fife, Scotland [7] [8].

The implications of expanding the rotors diameter are the increase of gravity loads on the blades and, additionally, transportation logistics challenges. Figure 1.10 illustrates examples of wind turbine blade transportation obstacles, related to blade size (a) and to tower diameter (b). Another challenge for manufacturers is that, by poorly scaling up the rotors, the cost can go up faster than the revenue generated by the increased capacity factor.

(a)

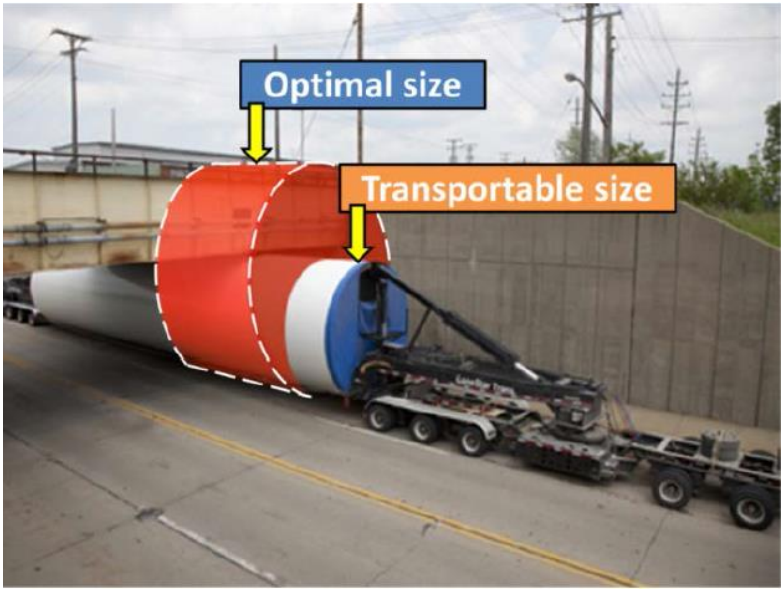

(b)

Figure 1.10 – Transportation challenges for large turbine blade. (Source: Keystone Tower Systems [9])

Modern wind turbines, however, have been increasingly cost-effective and more reliable, and have scaled up in size to multi-megawatt power ratings. Research has helped facilitate this transition, through the development of longer, lighter rotor blades, taller towers, more reliable drivetrains, and performance-optimizing control systems. Furthermore, improved turbine performance has led to a more robust domestic wind industry that saw wind turbine technology exports grow from $16 million in 2007 to $488 million in 2014 [10].

Also, wind energy costs have been reduced, in the United States, from over 55 cents (current dollars) per kilowatt-hour (kWh) in 1980 to an average of 2.35 cents in 2014 [11].

1.2 Motivation

As seen in the previous section, wind technology has experienced a significant advance in terms of turbine productivity over the past few years, accompanied of cost reductions for new wind plants. Advanced technology based on composite blades applied on rotors optimized for lower wind speed sites has resulted in a new generation of machines with larger rotors and lower specific power. Therefore, the motivation for this research is to study the aerodynamic theories applied on large turbine blades designed for lower wind speeds and, in sequence, develop a Matlab® code for the calculation of in-plane stresses due to these aerodynamic loads on thin-walled composite blades of a large wind turbine.

1.3 Research Objectives

The primary objectives for this research are:

1) To study the aerodynamic theories applied on horizontal axis wind turbine;

2) To implement a Matlab® code for the calculation of the aerodynamic loads in large wind turbine blades;

3) To investigate a robust procedure to calculate stresses in thin-walled cross section blades;

4) To apply the developed methodology in a case study of large wind turbine composite blade.

1.4 Outline of Subsequent Chapters

Chapter 2 approaches the research state of the art and the latest advances and new trends in wind turbine technology. Chapter 3 presents the fundamental theories on aerodynamics for horizontal axis wind turbines used in this work. Chapter 4 addresses particularities in the aerodynamics

of large wind turbines and details the model implementation to deal with them. Chapter 5 covers multilayer shell theories and Chapter 6 the mathematical model for stress analysis on thin-walled composite blades developed in this dissertation. Chapter 7 presents some results of stress analysis obtained with the developed code in a case study of large wind turbine composite blade. Finally, Chapter 8 details the conclusions extracted in this dissertation and highlights the scope for future work.

CHAPTER 2

LITERATURE REVIEW

This chapter presents a comprehensive literature review concerning the wind turbine blade developments. The topics are split into two major categories, namely i) The Research State of the Art, and ii) Advances and New Trends in Wind Turbine Technology.

2.1 The Research State of the Art

To solve a design or control problem of wind turbine blades, a typical way is to reduce the real, complex blade into a simple mechanical model that only depends on important parameters, and then analytical, semi-analytical and numerical methods are employed [12].

In earlier literature, an isolated blade was usually represented as a rotating rigid body. For example, Chopra and Dugundji [13] established a three-degrees-of-freedom analytical model (including rigid body flap, lead/lag and feather motion) for a rigid blade and studied the nonlinear dynamics of the blade. However, as the blades get more and more flexible with growing size of wind turbines nowadays, many flexible system models have been introduced for flexible blades, and the finite element method (FEM) has been widely used in modeling. For example, Lee et al. [14] considered horizontal axis wind turbine as a multi-flexible-system composed of rigid subsystems (hub and nacelle) and flexible subsystems (blade and tower), and established a blade model by using the FEM. By using the principle of virtual work in conjunction with the FEM, Baumgart [15] proposed a blade model in which the warping, extension and tilt effects of the cross section were included. Kallesøe [16] proposed an analytical model for blades with pitch action, in which the interactions among gravity, pitch action, varying rotor speed and blade motion were stressed. Ramakrishnan and Feeny [17] introduced a mathematical model for the lead/lag motion of a blade subjected to gravitational and

aerodynamic loading, and performed a perturbation analysis for the nonlinear dynamics of the blade in super and sub-harmonic resonances.

Given that, Li et al. [12] proposed an explicit formulation describing the nonlinear vibration of an isolated rotating blade with emphasis on structural damping, gravitational loading and aerodynamic loading. The structural damping induced by materials and fillers is expressed through the Kelvin–Voigt principle, i.e. strain and stress satisfy the relationship $\sigma = E\varepsilon + \bar{\eta}\dot{\varepsilon}$. The system consists of a rotating blade and four components of deformation including longitudinal vibration (named axial extension), out-of-plane bend (named flap), in-plane/edgewise bend (named lead/lag) and torsion (named feather). It is assumed that the center of mass, shear center and aerodynamic center of a cross section all lie on the chord line, and do not coincide with each other, as shown in Figure 2.1. Gravitational loading and aerodynamic loading are considered as distributed forces and moments acting on blade sections and a set of partial differential equations governing the coupled, nonlinear vibration is established by applying the generalized Hamiltonian principle.

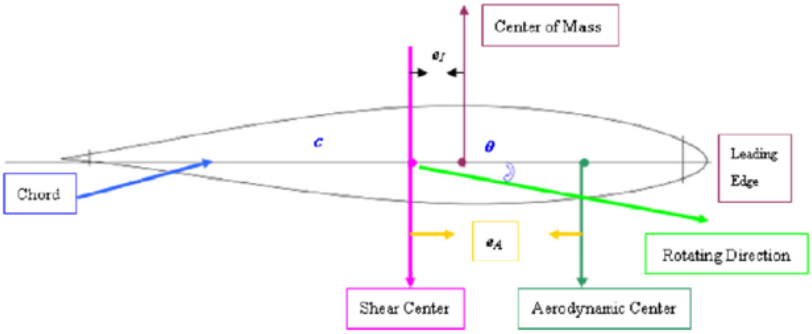

Figure 2.1 – Center of mass, shear center and aerodynamic center of a cross section (Source: Li et al. [12])

The model was then verified by previous models and it was found by Li et al. [12] that, by employing it, some design and control problems of blades, such as aeroelastic stability and nonlinear dynamics, can be handled via analytical and numerical techniques.

Another related study [18] claims that to study and analyze a blade's structural dynamics and aeroelasticity, it is essential to accurately and rapidly calculate its cross-sectional properties. However, that turns out to be also inherently difficult due to its complex structures, including several layers of composite materials with shear webs. Various methods have been proposed for calculating the cross-sectional properties of wind turbine blades, ranging from the simple two-dimensional (2D) lamination theory to detailed finite-element and 3D laminate techniques, which, despite their ability for accurate stress and displacement analysis, cannot directly yield the cross-sectional properties of wind turbine blades; they rely on computationally post-processing of force-displacement data. Also, these 3D laminate theories cannot accurately estimate the torsional stiffness, which is over estimated by as much as 50-80 times using these theories. The torsional stiffness is hard to evaluate because it is significantly affected by shear web and warping effects, which are difficult to model. And this is particularly true for wind turbine blades, because they commonly use a symmetrical cross-section with several shear webs (see Figure 2.2).

Compared to the finite element techniques and 3D laminate theories, Classical Lamination Theory, which is an extension of the classical plate theory to laminated plates, is fast and reasonably accurate [18]. CLT can be used to combine properties and the angle of each ply in a pre-specified stacking sequence to calculate the overall effective performance for a laminate structure. Based on several reasonable assumptions, such as in-plane stress and linear strain, CLT transfers a complicated 3D elasticity problem to a solvable 2D problem.

For a closed thin-walled cross-section, Bredt-Batho shear flow theory (BSFT) can be used to determine the torsional stiffness of the cross-section [18]. BSFT is developed based on the assumption that the torsional stress is uniformly distributed across the thickness of the cross-section, which is acceptable for most thin-walled cross-sections [19]. BSFT also implicitly includes the dominant warping effects and it can provide reasonable results for the torsional stiffness, but this theory is developed for a single-cell cross-section. In order to apply BSFT to a

practical wind turbine blade cross-section with shear webs, an extension of BSFT to cover multi-cells is required.

Given this, L. Wang et al. [18] presented a new mathematical model for calculating the cross-sectional properties of composite blades by incorporating classical lamination theory (CLT) with extended Bredt-Batho shear flow theory (EBSFT).

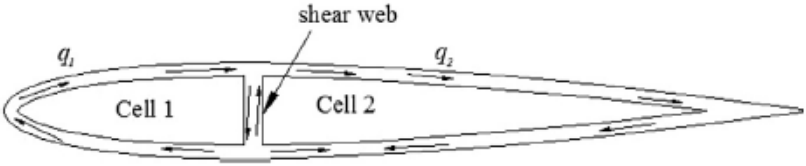

Figure 2.2 – Blade cross-section with one shear web. (Source: L. Wang et al. [18])

Figure 2.3 shows the flow chart for the new methodology developed by L. Wang et al. [18].

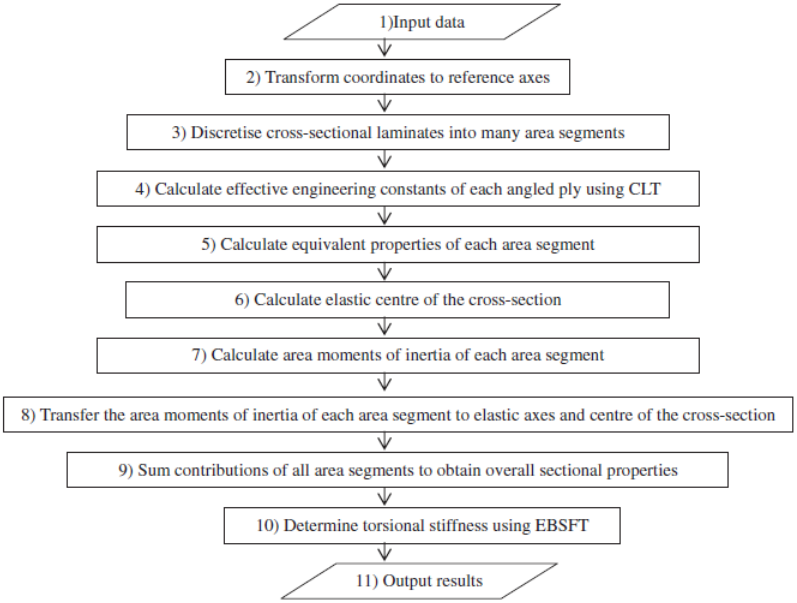

Figure 2.3 – Flow chart of the mathematical model. (Source: L. Wang et al. [18])

Based on the above, a Matlab-based cross-sectional analysis program, named as CBCSA (Composite Blade Cross-Section Analysis), was developed. CBCSA allows arbitrary geometric shape and internal structural layout of the blade. It directly extracts the cross-sectional properties of the blade, such as axial stiffness EA, flap wise stiffness EI_X, edgewise stiffness EI_Y, mass per unit length μ and torsional stiffness GJ, and runs fast. Moreover, the shear web and warping effects are taken into account by CBCSA due to the usage of EBSFT in the calculation of torsional stiffness [18].

After performing a series of benchmark calculation tests for isotropic and composite blades, the results showed that good agreement was achieved comparing the data from experiment with FEA, that CBCSA can extract the cross-sectional properties much faster than a FEM, usually in a fraction of a second, and that CBCSA provides an improved accuracy of torsional stiffness calculation due to the consideration of the shear web effects by using EBSFT [18].

Another important aspect of a modern variable-speed wind turbine is its power curve, which is typically characterized by three different operating conditions: cut-in, rated and cut-out wind speeds, as shown in Figure 2.4.

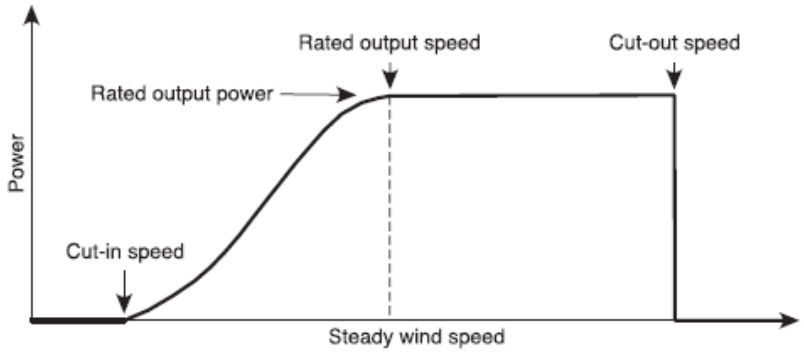

Figure 2.4 – Cut-in, rated and cut-out wind speeds. (Source: Capuzzi et al. [20])

Usually, a wind turbine blade is designed to maximize its aerodynamic performance below rated speed and to withstand extreme loads above it

[20]. Owing to the increased mass and loads associated with larger wind turbines, some works focus on reducing weight by performing structural optimizations and some lay emphasis on alleviating extreme aerodynamic loads by considering flexible airfoil sections. Therefore, one can, in a passive adaptive manner, achieve the alleviation of extreme aerodynamic loads by exploiting the capabilities that structural anisotropy and geometrically induced coupling provide, such as designing the main spar's torsional and bend-twist stiffnesses to induce a nose-down rotation. This strategy causes a reduction of the angle of attack and, consequently, a reduction of the aerodynamic forces acting on the profiles for higher wind speeds. On the other hand, below rated speed, where the loads are not critical and the power maximization is the main goal, this working principle causes a power loss [20].

Another strategy is to explore a towards stall bend-induced twist (nose-up), which causes a decrease of the section twist. This solution enhances the annual energy production (AEP), but causes a notable increase of gust-induced and fatigue loads [20]. Opposed to classic designs, where the total twist is given by a pre-twist plus a pitch angle, both these strategies add an elastically-induced twist to the total twist.

Given that, Capuzzi et al. [20] introduced a new aeroelastic approach to the design of large-scale wind turbine blades aiming an adaptive blade that can conciliate an increase of the yielded power with an alleviation of the extreme aerodynamic loads.

In the first part of their work, they use a current blade as a baseline for an aerodynamic analysis aimed at maximizing the turbine's yielded power below rated wind speed by allowing the angles of attack of the sections along the blade length to adapt to different wind speeds. This adaptation consists of a nose-down rotation, but now the elastically-induced twist is no longer a monotonic function of the radial position. Upon bending, moving from root to tip, the induced twist first decreases the angles of attack, then, outwards, the trend is inverted and the angles of attack increase again.

The aerodynamic analysis is performed to identify the theoretically ideal aeroelastic response of a reference blade. By doing so, the distributions of twist that maximize the power yielded at different wind speeds are obtained. Then, noting that the total twist is the sum of pre-twist, pitch angle and elastically-induced twist, a distribution of elastic twist that adaptively varies the blade's total twist to align with the ideal aeroelastic response, while also providing gust load alleviation, is identified.

Capuzzi et al. [21] then exploit material and structural bend-twist couplings in the main spar to induce the appropriate differential blade twist, section by section, while bending flap-wise. Here, two types of bend-twist coupling are exploited: geometric coupling, obtained by curving the blade's planform, and material coupling, by building unbalanced composite laminates into the structure. The adaptive behavior is achieved by merging these bend-twist coupling capabilities of off-axis composite plies and of a swept blade planform. The underlying principle here consists of using the nose-down bend-twist coupling of a curved blade (swept backward) and then reducing it by suitably skewing the fibers in the second half of the blade, through tow steered laminates, as illustrated in Figure 2.5. The steering of the fiber is essential in this case because it allows the variation of the local material bend-twist coupling and the required inversion of the induced twist rate.

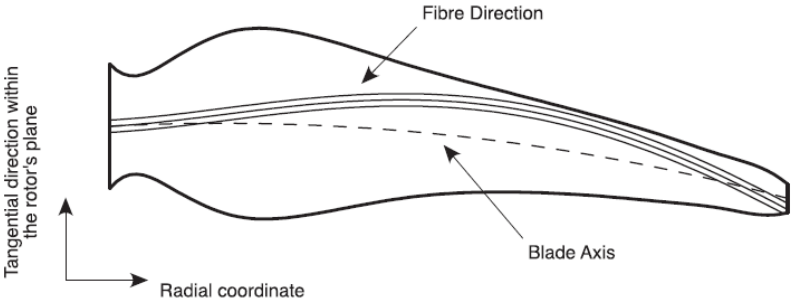

Figure 2.5 – Schematic fiber path over the curved blade planform. (Source: Capuzzi et al. [21])

In the remainder of the article, a demonstrative case study is proposed, where a realistic type of spar structure is designed to meet the targeted

adaptive capability and to fit within an existing reference blade, and a comparison between the power performance of this blade and of a conventional blade is made. As a result, it was shown that, by suitably tailoring the blade's elastic response to the aerodynamic pressure, it is possible to improve the turbine's annual energy production and, at the same time, alleviate extreme loading conditions due to gusts of wind. However, it must be pointed out that the structural analysis is simplified, considering only the elastic contribution of the main spar. Therefore, it cannot be known if the targeted distribution of twist could be achieved with a complete blade structure, including the aerodynamic shells. Furthermore, design constraints, such as strength and buckling, were not considered. According to Capuzzi et al. [21], these limitations must be addressed in future work to investigate whether the adaptive concept is possible with a more practical blade model. Also, to develop a comprehensive comparison between the proposed adaptive solution and other passive concepts, it is required to assess additional load alleviation capability.

2.2 Advances and New Trends in Wind Turbine Technology

While a previous focus of the industry was increasing the total nameplate capacity of wind turbines, as mentioned in the previous chapter, the focus has shifted to the capacity factor of the turbine, which helps keeps energy cost low by providing the most possible power. Ten years ago, the turbine was at about 25% capacity factor [22]; nowadays, 40 to 50% can be reached. And some say that 60 percent is within reach [23]. By improving the capacity factors, one enables to go into more and more locations where the wind is lower.

Besides the focus on capacity factor, the industry has been investing also on the improvement of individual components used in turbines, both electronics and gearboxes, in order to increase reliability. GE, for example, is looking at ways to harden gears as well as different types of bearings and bearings configuration [22].

Challenges also arise in offshore production, where companies used to take the same wind turbine used on land and install it offshore. Now, this has driven different aspects of the design of the wind turbines, with one of the main decisions being using direct drive technology. One example is the Haliade 150, Figure 2.6, a 6 MW turbine with a 150-meter rotor that has been designed from the very beginning to operate in offshore conditions [22]. Companies are also looking at the use of floating wind turbines, which use floating structures instead of requiring wind towers be set into a foundation under water.

Figure 2.6 – Haliade 150-6MW turbine. (Source: Alstom [24])

As companies look to make more sophisticated wind turbine technology, more and more sophisticated tools are required. So another area that is continuously enhanced is 3D modeling technology, where companies are able to use softwares to set up the blade in a virtual lab. Designers can then vary the blade geometry, blade twist, yaw angle, angle of attack and wind velocities and see the lift and drag coefficients across the blade on both top and bottom surfaces [22].

Modeling software can still be used in more than blade design, such as for siting wind power projects. Buildings, hills and even trees can change wind turbine behavior, so software use can help choose the correct installation for a given wind farm. Although siting may be less important in offshore wind power projects, the software can be used to help decide

the best way to run power onshore as well as determine the right strategy for installing the tower into the ocean floor [22].

The technology can also be used for a variety of other simulations, including manufacturing components, as well as monitoring the potential performance of generators and components, performing structural analysis or looking at electronic controllers.

A trend in large wind turbine technology are modular blades [25]. As mentioned in the previous chapter, one of the main challenges for large wind turbines is the transportation logistics. Hence, portability becomes a huge issue when it comes to the cost of wind energy. Also, assuming no changes in design, materials or construction methods, the amount of generated power increases with blade length in proportion to the square of the turbine rotor's diameter, but blade mass increases in proportion to the cube of the diameter. This means the rate of mass increase exceeds the rate of generated power increase as blades get longer. As a result, longer, exponentially heavier blades vastly increase transportation and installation difficulties and cascade mass and cost increases throughout the turbine/tower system. In that scenario, Gamesa gathered efforts to develop the world's first commercial segmented composite blade to be applied on the Gamesa's G128 turbine [26]. With blades 62.5 m long, the turbine generates up to 5 MW of power, but its blades weigh less than blades used on standard 100 m rotors and are as easy to install as the much shorter blades used on 2 MW systems.

In Figure 2.7, a detailed illustration of the Gamesa's INNOBLADE segmented design for the G128 Turbine is presented. In Figure 2.8, one can see a real photo of the solution for the joint. And, in Figure 2.9, one can see blade segments awaiting assembly.

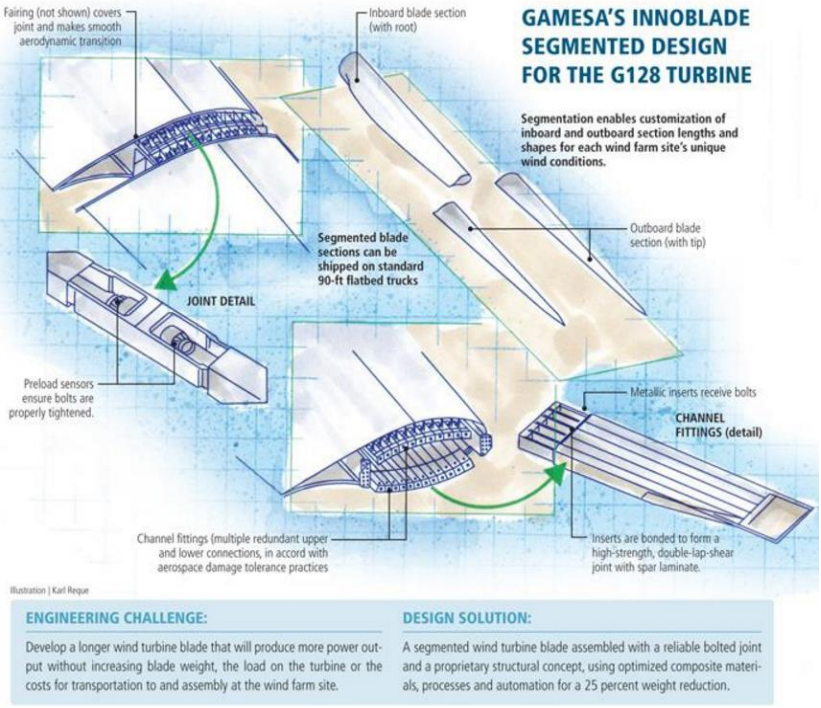

Figure 2.7 – Gamesa's Innoblade Segmented Design for the G128 Turbine. (Source: Gamesa [26])

Figure 2.8 – Metallic fittings are bonded into the spar laminate of each blade segment and then bolted together to join the two segments. (Source: Gamesa [26])

Figure 2.9 – Blade segments delivered to a wind farm await assembly. (Source: Gamesa [26])

Another trend are the gigantic blades longer than two football fields that could help bring offshore 50 MW wind turbines to the United States and the world. Product of the Sandia National Laboratories' research on the extreme-scale Segmented Ultralight Morphing Rotor (SUMR), these new giant turbines require a rotor blade more than 200 meters long, two and a half times longer than any existing wind turbine blade [27].

Most current U.S. wind turbines produce power in the 1 to 2 MW range, with blades about 50 meters long, while the largest commercially available turbine is rated at 8 MW with blades 80 meters long [28].

While a 50 MW horizontal wind turbine is well beyond the size of any current design, studies show that load alignment can dramatically reduce peak stresses and fatigue on the rotor blades. This could reduce costs and allow construction of blades big enough for a 50 MW system [28].

These exascale turbines would be sited downwind, unlike conventional turbines that are configured with the rotor blades upwind of the tower (Figure 2.10). This is because conventional upwind blades are expensive to manufacture, deploy and maintain beyond 10-15 MW [28]. They must be stiff, to avoid fatigue and eliminate the risk of tower strikes in strong gusts of wind. Those stiff blades are heavy, and their mass, which is directly related to cost, becomes even more problematic at the extreme scale due to gravity loads and other changes.

a) b)

Figure 2.10 – Conceptual comparison of: a) a conventional upwind rotor, and b) a downwind aligned rotor (wind direction from left). (Source: Loth et al. [29])

At dangerous wind speeds, these new gigantic blades are stowed and aligned with the wind direction, reducing the risk of damage. At lower wind speeds, the blades spread out more to maximize energy production, as shown in Figure 2.11.

SUMR's load-alignment is bio-inspired by the way palm trees move in storms. The light weight, segmented trunk approximates a series of cylindrical shells that bend in the wind while retaining segment stiffness. This alignment radically reduces the mass required for blade stiffening by reducing the forces on the blades [28].

Also, these turbine blades could be more easily and cost-effectively manufactured in segments, avoiding the unprecedented-scale equipment needed for transport and assembly of blades built as single units.

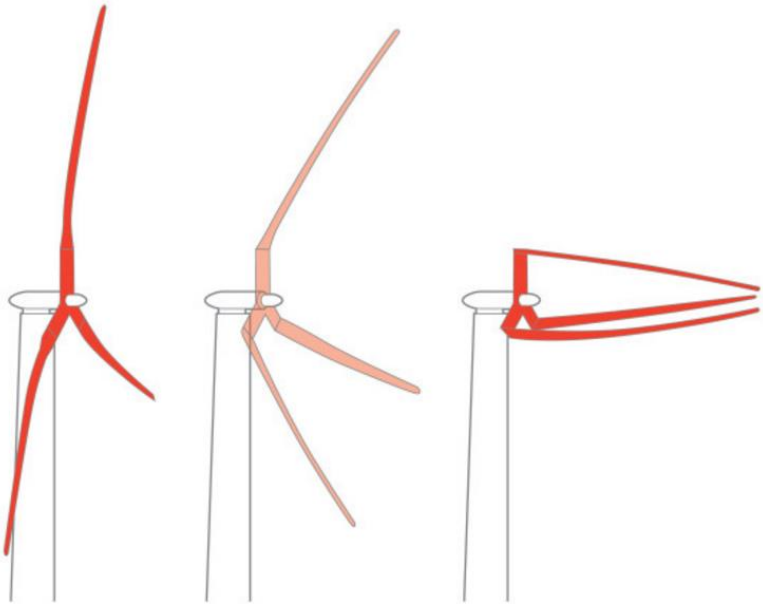

Figure 2.11 – Blades alignment with the wind direction. (Source: Sandia National Laboratories [28])

2.3 Concluding Remarks

There are many challenges posed by extreme-scale systems that will need to be addressed through technological innovation and demonstration in the next 10-20 years [29]. The technological advances made with wind turbines though have resulted in clear bottom line: Wind power is more efficient and affordable than it has ever been, which has helped drive its

popularity along with power prices and incentives such as the U.S. production tax credit. As quickly as wind technology has developed in the past 10 years, some specialists expect that pace to at least continue and possibly accelerate.

CHAPTER 3

FUNDAMENTAL THEORIES ON AERODYNAMICS FOR HORIZONTAL AXIS WIND TURBINES

This chapter describes an aerodynamic model for horizontal axis wind turbines, whose objective is to predict the main aspects of the turbine's performance and to provide a means of dimensioning the geometric characteristics for a first approximation of an optimized design. This analytical model is constructed incrementally, starting from the simplified model of an actuator disc, followed by the inclusion of the rotor rotation and by the introduction of the aerodynamic characteristics of the turbine blade, which is discretized. Then, the last two models are combined into the Blade Element Momentum (BEM) Theory, which, by taking the blade geometry into consideration, will enable the calculation of the turbine performance. And finally, taking into account the airfoil (profile) used, the chord and twist distributions along the blade span that maximize the power extracted from the wind are calculated.

3.1 Actuator Disc and Betz Limit

As a first approach to the design of HAWT blades, the turbine rotor can be modeled as an actuator disc, as suggested by Betz, which enables one to predict the performance of an ideal turbine, as well as, the effect of its operation in the local wind flow [30].

The turbine, as shown in Figure 3.1, is represented by a uniform actuator disc (or a rotor with an infinite number of blades) that creates a pressure discontinuity in the stream-tube passing through it. Upstream of the disc, the stream-tube has a cross-sectional area smaller than that of the disc and, downstream, a larger one. The expansion of the stream-tube is because the mass flow rate must be the same everywhere. The mass of air that passes through a given cross-section of the stream-tube in a unit

length of time is ρAU, where ρ is the air density, A is the cross-sectional area of the tube and U is the wind velocity. This theory considers an incompressible, homogeneous, steady and one-dimensional flow, and does not consider friction or wake rotation [30].

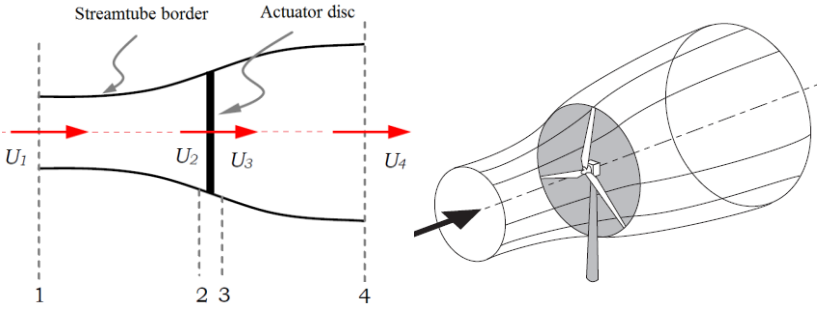

(a) (b)

Figure 3.1 – Actuator disc model of a wind turbine. (Source: (a) Manwell [30], (b) Burton [2])

Here, sections 1 and 4 are sufficiently far apart so that the pressures $p_1 = p_4 = p_\infty$ and the wind speed $U_1 = U_\infty$, where the index ∞ indicates the point at which the flow is unaffected by the presence of the turbine. Moreover, by continuity, $A_2 = A_3 = A$ and $U_2 = U_3$.

Applying the conservation of linear momentum to the control volume enclosing the system, one can find the resultant force applied on the flow. This force is the reaction to the thrust force T that the wind exerts on the turbine, which produces mechanical energy to its rotation [30]:

$$T = U_1(\rho AU)_1 - U_4(\rho AU)_4 \tag{3.1}$$

For steady state flow, the conservation of mass dictates that $(\rho AU)_1 = (\rho AU)_2 = (\rho AU)_4 = \dot{m}$, where $\dot{m}$ is the mass flow rate. Hence:

$$T = \dot{m}(U_1 - U_4) \tag{3.2}$$

The thrust is positive so the velocity behind the rotor, U_4, is less than the free stream velocity, U_1. Considering that no work is done and that there are no losses on either side of the turbine rotor, the Bernoulli equation can be used in the two control volumes, before and after the actuator disc:

$$p_1 + \frac{1}{2}\rho {U_1}^2 = p_2 + \frac{1}{2}\rho {U_2}^2 \tag{3.3}$$

$$p_3 + \frac{1}{2}\rho {U_3}^2 = p_4 + \frac{1}{2}\rho {U_4}^2 \tag{3.4}$$

The thrust T can also be expressed as a function of the pressures, as the net sum of the forces on each side of the actuator disc:

$$T = A(p_2 - p_3) \tag{3.5}$$

If one solves for $(p_2 - p_3)$ using equations (3.3) and (3.4) and substitutes that into equation (3.5), one obtains:

$$T = \frac{1}{2}\rho A({U_1}^2 - {U_4}^2) \tag{3.6}$$

And equaling the equations (3.2) e (3.6), one obtains:

$$U_2 = \frac{U_1 + U_4}{2} \tag{3.7}$$

That is, the wind velocity at the rotor plane, using this simple model, is the average of the upstream and downstream wind speeds [30].

Now, if one defines the axial induction factor, a, as the fractional decrease in wind velocity between the free stream and the rotor plane, then:

$$a = \frac{U_1 - U_2}{U_1} \tag{3.8}$$

$$U_2 = U_1(1 - a) \tag{3.9}$$

$$U_4 = U_1(1 - 2a) \tag{3.10}$$

By examining the equation (3.10), one can see that as the axial induction factor increases from 0, the wind speed behind the rotor slows more and more until it reaches $U_4 = 0$ for $a = 1/2$, when the theory is no longer applicable.

Henceforward, $U_1 = U_\infty = U$ and the axial velocity on the rotor $U_2 = U(1 - a) = v_a$. One can now rewrite the equation (3.6) as:

$$T = \frac{1}{2}\rho A U^2[4a(1 - a)] \tag{3.11}$$

And the power extracted from the wind, P, is equal to the thrust times the velocity at the disc:

$$P = T.U(1 - a) = \frac{1}{2}\rho A U^3[4a(1 - a)^2] \tag{3.12}$$

Now one can define the turbine's Power Coefficient, C_P, a measure of the aerodynamic performance of the turbine, by representing the fraction of the power in the wind that is extracted by the rotor:

$$C_P = \frac{rotor\ power}{power\ in\ the\ wind} = \frac{P}{\frac{1}{2}\rho A U^3} = 4a(1 - a)^2 \tag{3.13}$$

The maximum of this function, that is, the maximum energy that can be extracted from the wind and converted into mechanical energy to rotate

the turbine rotor is determined by taking the derivative of C_P with respect to a and setting it to zero:

$$\frac{dC_P}{da} = 0$$

Which yields $a = 1/3$. Thereby:

$$C_{P,max} = \frac{16}{27} = 0.5926$$

This maximum value of C_P is known as the Betz limit and is the theoretical maximum that an ideal rotor can reach. However, there are still other factors that contribute to the reduction of the efficiency, such as the rotation of the wake behind the rotor, the finite number of blades and associated tip losses, non-zero aerodynamic drag and operation out of the optimal conditions [30].

Moreover, the Thrust Coefficient, C_T, is defined as:

$$C_T = \frac{thrust\ force}{dynamic\ force} = \frac{T}{\frac{1}{2}\rho A U^2} = 4a(1-a) \qquad (3.14)$$

C_T reaches its maximum of 1 when the axial induction factor $a = 0.5$ and the downstream velocity is zero.

3.2 Rotor Disc Theory

The second step in the construction of the analytical model is the inclusion of the rotor rotation and the conservation of angular momentum [31].

In a horizontal axis turbine that rotates with angular velocity Ω, energy is extracted from the wind by the torque Q applied on the rotor blades by the air passing through it. As a reaction to the torque applied on the rotor, the airflow behind the rotor (downstream) also develops a rotational

velocity ω, which has the opposite direction to Ω. This so called wake rotation is represented in the Figure 3.2.

The generation of rotational kinetic energy in the wake results in less energy extraction by the rotor than would be expected without wake rotation.

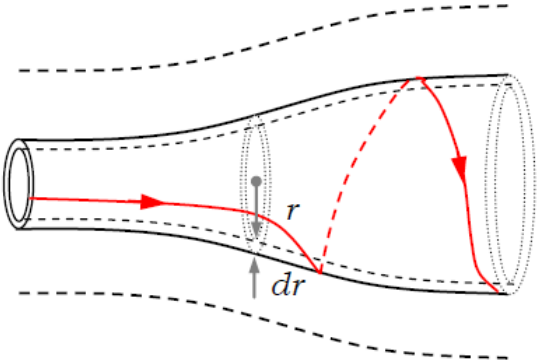

Figure 3.2 – Stream tube model of flow behind rotating wind turbine blade. (Source: Manwell [30])

Defining a ring-shaped control volume of radius r and thickness dr, represented in the Figure 3.2, that moves with the angular velocity of the blades, one finds an area $dA = 2\pi r dr$, in which the pressure, the wake rotation and the induction factors are function of the radius r. Here, the considerations of an infinite number of blades and that there are no energy losses are still maintained.

Defining now the angular induction factor a' in function of the angular velocity of the blades Ω and of the induced wake rotation ω:

$$a' = \frac{\omega}{2\Omega} \tag{3.15}$$

The tangential velocity incident on the blades is:

$$v_t = r\Omega(1 + a') \tag{3.16}$$

And the torque applied on the flow by the ring dr is:

$$dQ = \frac{1}{2}\rho.dA.U(1-a)4\Omega a' r^2 = \rho.U.4a'(1-a)\Omega r^3\pi.dr \tag{3.17}$$

Since the deduction is still valid considering the wake rotation, Eq. (3.11) can be rewritten for the same control volume to determine the thrust generated by a blade element:

$$dT = \rho U^2 4a(1-a)\pi r dr \tag{3.18}$$

The torque exerted by the turbine generator will also be dQ, so the power extracted from the wind is:

$$dP = \Omega dQ = \frac{1}{2}\rho.dA.U(1-a)4\Omega^2 a' r^2 \tag{3.19}$$

Taking the ratio between the tangential velocity on the blade tip and the free stream wind speed U, one defines the tip speed ratio:

$$\lambda = \frac{\Omega R}{U} \tag{3.20}$$

The same goes to the local speed ratio, for an intermediate radius r or fraction of the radius $\mu = r/R$:

$$\lambda_r = \frac{\Omega r}{U} = \frac{\lambda r}{R} = \lambda.\mu \tag{3.21}$$

Thus, the power extracted from the wind, given by the Eq. (3.19), can be rewritten in function of λ and λ_r:

$$dP = \frac{1}{2}\rho A U^3 \left[\frac{8}{\lambda^2} a'(1-a)\lambda_r^3 d\lambda_r\right] \tag{3.22}$$

The incremental contribution to the power coefficient, dC_P, from each annular ring is given by:

$$dC_P = \frac{dP}{1/2\,\rho A U^3} \tag{3.23}$$

That, integrating, yields:

$$C_P = \frac{8}{\lambda^2}\int_{\lambda_c}^{\lambda} a'(1-a)\lambda_r^3 d\lambda_r \tag{3.24}$$

Where $\lambda_c = \lambda r_c/R$ is the local speed ratio on the turbine hub. The analytical integration of this equation involves writing a and a' in function of λ_r, which will not be detailed here.

In general, the wake rotation and the associated energy loss are greater when the generated torque increases. That is why low speed and high torque turbines have a lower maximum efficiency than turbines with higher rotation speeds, as shown in the Figure 3.3.

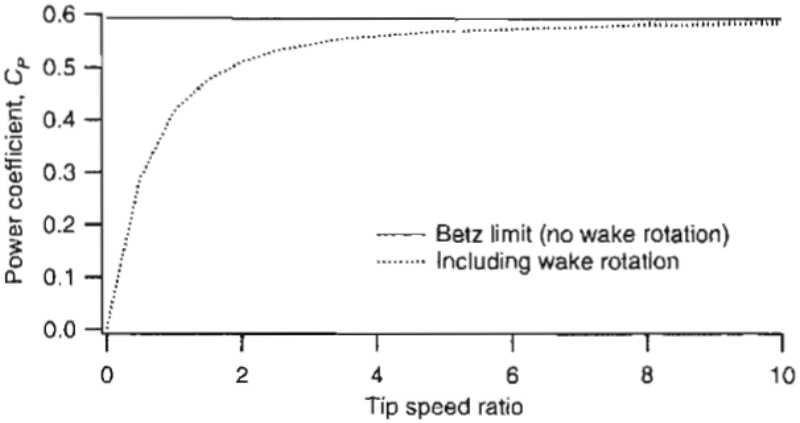

Figure 3.3 – Theoretical maximum power coefficient as a function of tip speed ratio λ for an ideal horizontal axis wind turbine, with and without wake rotation. (Source: Manwell [30])

3.3 The Blade Element

Now, taking into account the profile of the airfoil used, the aerodynamic characteristics of each blade element are introduced in the analysis.

A blade element is defined as a section of length dr of the total length R of the blade, located a distance r from the rotation axis, usually defined by the fraction $\mu = r/R$, and that has the following aerodynamic characteristics, as illustrated in the Figure 3.4:

- An aerodynamic profile;
- A chord c (distance between the leading edge and the trailing edge);
- A pitch angle β (angle between the chord and the rotation plane).

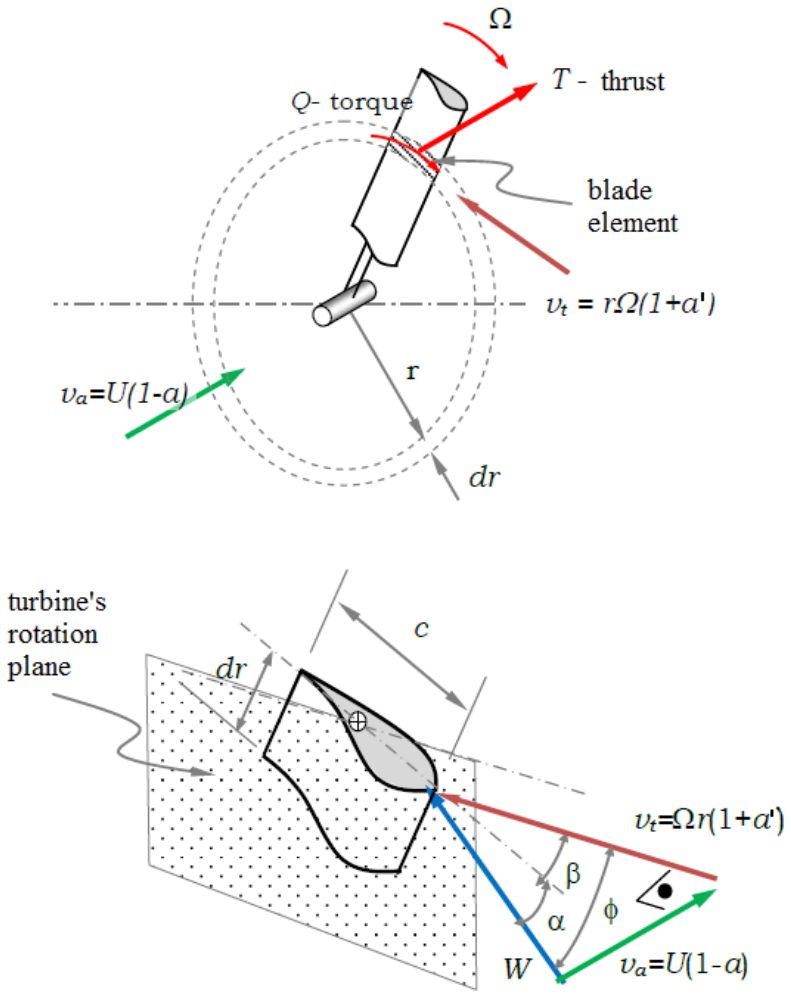

Figure 3.4 – Blade element variables.

Where:

- v_a – induced axial velocity (m/s);
- v_t – induced tangential velocity (m/s);
- W – local velocity of the resultant airflow (m/s);

- Ω – rotation velocity of the blade (rad/s);

- α – angle of attack (angle between the incoming airflow W and the chord c);

- ϕ – angle between the turbine rotation plane and the resulting wind direction.

3.4 Aerodynamic Forces on the Blade Element

In the blade element, the only present external forces are the lift L and drag D, in addition to the pitching moment M, applied in the aerodynamic center of the profile, and contained in the central plane of the element.

- The lift force L is consequence of the unequal pressure on the upper and lower airfoil surfaces and is defined to be perpendicular to the direction of the incoming airflow;

- The drag force D is due both to viscous friction forces at the surface of the airfoil and to unequal pressure on the airfoil surfaces facing toward and away from the incoming flow, and is defined to be parallel to the direction of the incoming airflow;

- The pitching moment M is defined to be about an axis perpendicular to the airfoil cross section.

These external forces and pitching moment acting on the airfoil cross section are shown in the Figure 3.5.

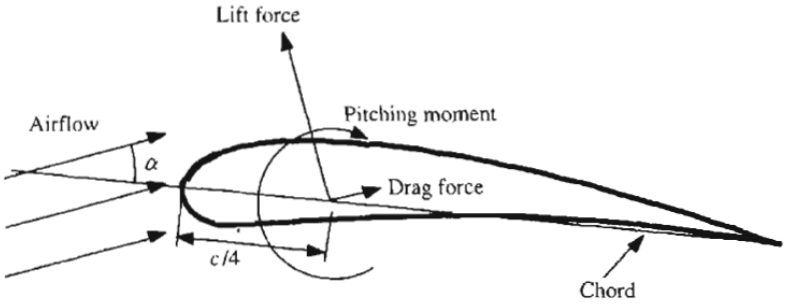

Figure 3.5 – Aerodynamics forces acting on the airfoil. (Source: Manwell [30])

Aerodynamic forces are normally defined via adimensional coefficients, whose lower-case index denotes that this is a value for the two-dimensional case, that is, by unit length dr:

$$C_l = \frac{L/dr}{1/2\,\rho W^2 c} \tag{3.25}$$

$$C_d = \frac{D/dr}{1/2\,\rho W^2 c} \tag{3.26}$$

$$C_m = \frac{M/dr}{1/2\,\rho W^2 c^2} \tag{3.27}$$

Where:

- C_l – Lift Coefficient;
- C_d – Drag Coefficient;
- C_m – Pitching Moment Coefficient;

The use of these adimensional coefficients allows their values to be determined independently of the chord c and of the airspeed U, depending only on the angle of attack α.

The determination of the aerodynamic coefficients is done in function of α from the polar curves, which are obtained for each airfoil profile type via experimental data in a wind tunnel or via CFD calculations [31].

Obtaining the curves is difficult because they have variations depending on the Reynolds number Re, which is defined locally for each blade element:

$$Re = \frac{W.c}{\nu} \tag{3.28}$$

Where:

- c – chord (m);
- ν – kinematic viscosity of the air (m^2/s);
- W – resulting velocity of the incident flow (m/s).

The Reynolds number physically represents the ratio between the intensity of the fluid inertial force and the viscous force and it corresponds to the vector sum of the axial and tangential velocities, v_a and v_t, respectively.

$$W = \sqrt{{v_t}^2 + {v_a}^2} = U\sqrt{\lambda_r(1 + a')^2 + (1 - a)^2} \tag{3.29}$$

Since Re is a function of W and c, which are variables to be determined, usually polar curves are obtained with an estimated Reynolds number by assuming that it will have little influence on the result [31]. In the present work, however, a different approach was taken, as will be presented in the next chapter.

Assuming that the three adimensional coefficients mentioned earlier were determined, one then calculates the forces acting on the element of length dr, as shown in the Figure 3.6:

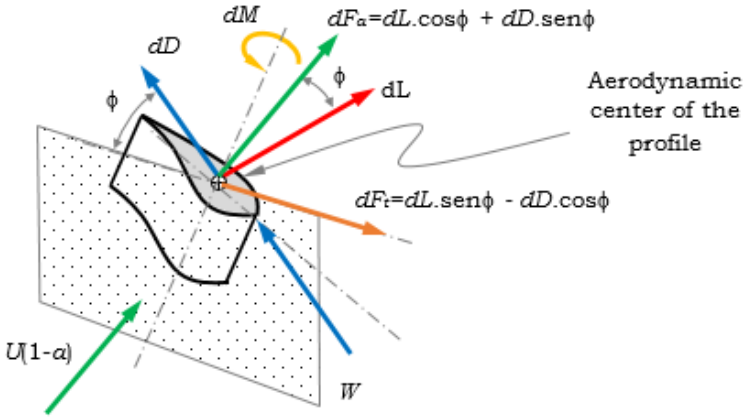

Figure 3.6 – Aerodynamic forces acting on the blade element.

Where:

- dL – lift force (N/m);
- dD – drag force (N/m);
- dM – pitching moment (N.m/m);
- dF_a – resulting force in the axial direction;
- dF_t – resulting force in the tangential direction.

All forces are applied on the aerodynamic center of the profile, which by its definition implies a constant moment dM in function of α and at approximately 25% of the chord for most airfoils [30].

From equations (3.25) to (3.27), the loads acting on a blade element are:

$$dL = \frac{1}{2}\rho W^2 c C_l dr \tag{3.30}$$

$$dD = \frac{1}{2}\rho W^2 c C_d dr \tag{3.31}$$

$$dM = \frac{1}{2}\rho W^2 c^2 C_m dr \tag{3.32}$$

Resulting in both axial and tangential components of the forces applied to the blade element:

$$dF_a = dL.\cos\phi + dD.\sin\phi \tag{3.33}$$

$$dF_t = dL.\sin\phi - dD.\cos\phi \tag{3.34}$$

The thrust dT and the torque dQ applied on the blade element can also be calculated for the ring of radius r containing B elements, B being the number of turbine blades:

$$dT = B\frac{1}{2}\rho W^2 c(C_l\cos\phi + C_d.\sin\phi)dr \tag{3.35}$$

$$dQ = B\frac{1}{2}\rho W^2 c(C_l\sin\phi - C_d.\cos\phi)dr.r \tag{3.36}$$

Introducing the local blade solidity parameter σ_r as the ratio between the total area of the elements in r and the area of the ring swept by them:

$$\sigma_r = \frac{Bc}{2\pi r} \tag{3.37}$$

And substituting the Eqs. (3.37) and (3.42) into the Eqs. (3.35) and (3.36), one gets the thrust dT and the torque dQ applied on the blade element:

$$dT = \sigma_r \pi\rho\left[\frac{U(1-a)}{\sin\phi}\right]^2 (C_l\cos\phi + C_d.\sin\phi).r.dr \tag{3.38}$$

$$dQ = \sigma_r \pi \rho \left[\frac{U(1-a)}{\sin\phi}\right]^2 (C_l \sin\phi - C_d.\cos\phi).r^2.dr \qquad (3.39)$$

Finally, some useful trigonometric relations are obtained:

$$\phi = \alpha + \beta \qquad (3.40)$$

$$\tan\phi = \frac{U(1-a)}{\Omega r(1+a')} = \frac{1-a}{(1+a')\lambda_r} \qquad (3.41)$$

$$W = \frac{U(1-a)}{\sin\phi} \qquad (3.42)$$

3.5 The Blade Element Momentum Theory

The analysis here uses Momentum theory and Blade Element Theory. Momentum Theory refers to a control volume analysis of the forces at the blade based on the conservation of linear and angular momentum. Blade Element Theory refers to an analysis of forces at a section of the blade, as a function of blade geometry. The results of these approaches can be combined into what is known as Blade Element Momentum (BEM) Theory. This theory can be used to relate blade shape to the rotor's ability to extract power from the wind [30].

The aerodynamic forces calculated for each blade element, together with the equations obtained from the linear and angular momentum theory, finally allow to obtain the necessary relations for the determination of the induction factors a and a', from which one will determine the optimal design and the actual efficiency of the turbine.

According to Burton [2] and Manwell [30], one can simplify the calculations by considering the Drag Coefficient $C_d = 0$, without bringing any significant errors for the values of a and a'.

Thus, equating respectively the relations (3.17) and (3.18), derived from the linear and angular momentum theory, with the (3.38) and (3.39), from the blade element theory, and considering $C_d = 0$, one obtains the following relationships:

$$\frac{a'}{1-a} = \frac{\sigma_r C_l}{4\lambda_r \sin\phi} \tag{3.43}$$

$$\frac{a}{1-a} = \frac{\sigma_r C_l \cos\phi}{4sin^2\phi} \tag{3.44}$$

After some algebraic manipulation and replacing the trigonometric relation (3.41), one can get:

$$a = 1 \Big/ \left[1 + \frac{4sin^2\phi}{\sigma_r C_l \cos\phi}\right] \tag{3.45}$$

$$a' = 1 \Big/ \left[\frac{4\cos\phi}{\sigma_r C_l} - 1\right] \tag{3.46}$$

From these equations, the values of a and a' can be determined iteratively from λ_r, from known geometric parameters c, β and σ_r and from the polar curve of the Lift Coefficient $C_l(\alpha)$ for an airfoil profile in the following manner [30]:

1. Estimate initial values for a and a';
2. Calculate the angle of the incident flow ϕ by the equation (3.41);
3. Calculate C_l from the polar curve at $\alpha = \phi - \beta$;
4. Update a and a' by the equations (3.45) and (3.46);

5. Repeat steps 2-4 until the convergence of a and a'.

Having determined the induction coefficients for all elements, other parameters such as incident wind speed W and blade efficiency can be determined.

It should be noted that this calculation is done assuming a Reynolds number that is not exactly known when resorting to the polar curve of C_l, as described in the previous section.

When a and $a'$are known for all of the blade elements, each one being characterized by λ_r, the turbine power coefficient can be calculated by the following equation:

$$C_P = \frac{P}{P_{wind}} = \frac{\int_{r_c}^{R} \Omega \, dQ}{\frac{1}{2}\rho\pi R^2 U^3} \tag{3.47}$$

Although the induction factors were calculated excluding the effect of the drag force, this component should now be introduced into the calculation of the efficiency:

$$C_P = \frac{8}{R^4}\lambda^2 \int_{r_c}^{R} a'(1-a)r^3 \left[1 - \frac{C_d}{C_l}\cot\phi\right] dr \tag{3.48}$$

Or, changing the integration variable, with $dr = \frac{R}{\lambda} d\lambda_r$:

$$C_P = \frac{8}{\lambda^2} \int_{\lambda_c}^{\lambda} a'(1-a){\lambda_r}^3 \left[1 - \frac{C_d}{C_l}\cot\phi\right] d\lambda_r \tag{3.49}$$

Another equivalent expression eliminates the dependence on induction factors a and a':

$$C_P = \frac{8}{\lambda^2}\int_{\lambda_c}^{\lambda} sin^2\phi(\cos\phi - \lambda_r \sin\phi)(\sin\phi + \lambda_r \cos\phi)\left[1 - \frac{C_d}{C_l}\cot\phi\right]{\lambda_r}^2 d\lambda_r \tag{3.50}$$

From equation (3.48), one may also define the local efficiency of the blade element:

$$dC_P = \frac{8}{R^4}\lambda^2 a'(1-a)r^3\left[1 - \frac{C_d}{C_l}\cot\phi\right]dr \tag{3.51}$$

Similarly, the thrust T and torque Q will be obtained by integrating dT and dQ from equations (3.38) and (3.39).

3.6 Empirical Corrections

All the theory seen so far considered approximate conditions in which the flow is laminar and bidimensional. To obtain more realistic results, one introduces some corrections based on empirical relationships suggested in the literature.

1) Tip Losses

When considering a three-dimensional flow on a finite blade (or wing), it is necessary to introduce the effect of the flow around the blade tip, resulting from the pressure difference between the lower surface (high pressures, facing the flow) and the upper surface (low pressure), which reduces lift and hence power production near the tip.

This effect can be estimated more or less accurately by various methods. The most straightforward approach to use is one developed by Prandtl [30]. According to this method, a correction factor, named F, must be introduced into the previously discussed equations. This correction factor

is a function of the number of blades B, of the relative position of the element $\mu = r/R$ and of the angle of the local incident flow ϕ. Based on Prandtl's method, the correction factor due to tip losses is:

$$F_{tip} = \frac{2}{\pi}\cos^{-1}\left[\exp\left(-\frac{B(1-\mu)}{2\mu\sin\phi}\right)\right] \tag{3.52}$$

This correction factor varies between 1 (on the most part of the radius) and 0 (at the tip).

2) Root Losses

At the blade root, the presence of the hub implies that the calculated forces also should tend to zero in this region.

The phenomenon observed at the root and at the tip have different physical origins, but they are equivalent from the theoretical point of view, so the Prandtl function for losses at the tip can be adapted for the calculation of losses at the root. Based on this, the correction factor due to root losses is:

$$F_c = \frac{2}{\pi}\cos^{-1}\left[\exp\left(-\frac{B(\mu-\mu_c)}{2\mu\sin\phi}\right)\right] \tag{3.53}$$

The correction factor incorporating the losses at the hub and at the tip is thus given by the product of the two correction factors:

$$F(\mu) = F_{tip}(\mu).F_c(\mu) \tag{3.54}$$

The Figure 3.7 shows an example of a spanwise variation of combined tip and root losses factor for a three-blade turbine optimized for a tip speed ratio of six and with a blade root at 20% span.

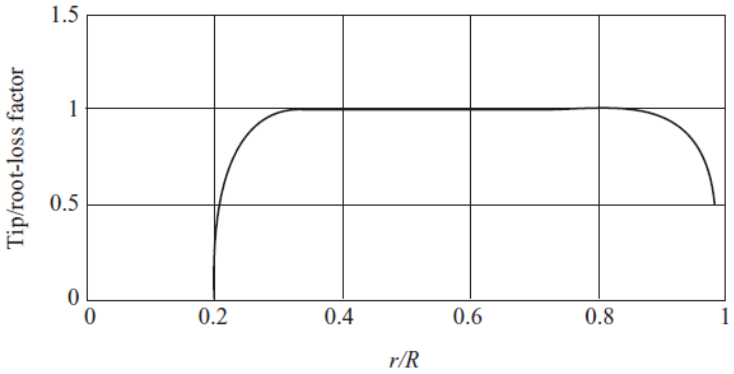

Figure 3.7 – Span-wise variation of combined tip/root loss factor for a three-blade turbine optimized for a tip speed ratio of six and with a blade root at 20% span. (Source: Burton [2])

The equations (3.17) and (3.18) deduced by the theory of linear and angular momentum become:

$$dQ = F\rho U 4a'(1-a)\Omega r^3 \pi dr \qquad (3.17)^*$$

$$dT = F\rho U^2 4a(1-a)\pi r dr \qquad (3.18)^*$$

The equations (3.45) and (3.46) of the BEM Theory become:

$$a = 1 \Big/ \left[1 + \frac{4F sin^2\phi}{\sigma_r C_l \cos\phi}\right] \qquad (3.45)^*$$

$$a' = 1 \Big/ \left[\frac{4F\cos\phi}{\sigma_r C_l} - 1\right] \qquad (3.46)^*$$

And the expressions for global and local power coefficient become:

$$C_P = \frac{8}{R^4}\lambda^2 \int_{r_c}^{R} F.a'(1-a)r^3 \left[1 - \frac{C_d}{C_l}\cot\phi\right] dr \qquad (3.48)^*$$

$$C_P = \frac{8}{\lambda^2}\int_{\lambda_c}^{\lambda} F.sin^2\phi(\cos\phi - \lambda_r \sin\phi)(\sin\phi + \lambda_r \cos\phi)\left[1 - \frac{C_d}{C_l}\cot\phi\right]{\lambda_r}^2 d\lambda_r \qquad (3.50)^*$$

$$dC_P = F.\frac{8}{R^4}\lambda^2 a'(1-a)r^3 \left[1 - \frac{C_d}{C_l}\cot\phi\right] dr \qquad (3.51)^*$$

3.7 Ideal Blade Element

So far, the adopted methodology sought to determine the aerodynamic characteristics of a generic blade element, such as its chord and torsion angle, but that are not necessarily aerodynamically optimum. Now, the analytical model is conducted to calculate the optimal values for these parameters, which correspond to those that allow for maximum aerodynamic efficiency [31].

The relation proposed by Manwell [30] takes into account the rotation of the wake, but ignores the Drag Coefficient ($C_d = 0$) and the tip losses ($F_{tip} = 1$).

For each element, considering its relative location $\mu = r/R$, the type of profile used (polar curve) and tip speed ratio parameters, one determines the optimum angle ϕ that is obtained by calculating the maximum of the function given by equation (3.50). This maximum is obtained analytically by deriving the function with respect to ϕ, which gives:

$$\phi = \frac{2}{3}\tan^{-1}\left(\frac{1}{\lambda\mu}\right) \qquad (3.55)$$

Then, by examining the polar curves, one defines the ideal angle of attack of the airfoil profile, α_{design}, as the angle for which the ratio C_l/C_d is maximum. Thus, one can determine the ideal torsion angle:

$$\beta = \phi - \alpha_{design} \tag{3.56}$$

Now, in order to obtain the ideal chord for each element, one uses the relations obtained with the BEM Theory and takes the C_l correspondent to α_{design}:

$$c = \frac{8\pi\mu R}{BC_l}(1 - \cos\phi) \tag{3.57}$$

It should be noted that, by considering $C_d = 0$, Eq. (3.55) defines a ϕ independent from the aerodynamic characteristics of the element. Therefore, although an optimum blade element is dimensioned for this value of ϕ, it is only approximate [31].

Finally, it must be emphasized once again that, in this approach, it is necessary to resort to the airfoil profile polar curves to determine the α_{design}, and therefore are again encountered difficulties due to the non-exact knowledge of the Reynolds number. This issue is addressed in the next chapter.

CHAPTER 4

CONSIDERATIONS IN AERODYNAMICS FOR LARGE WIND TURBINE

This chapter addresses the complexity of the fluid dynamics for large wind turbines and the problem regarding the obtention of Reynolds experimental data. Following that, one discusses an iterative procedure for determining Reynolds that seeks to eliminate the dependence on experimental data. Finally, the chapter ends with the details of the model implementation.

4.1 The Complexity of the Fluid Dynamics Problem

Within the field of aerodynamics, one of the main difficulties encountered in the analysis of wind turbines is to accomplish accurate and efficient numerical simulations of flow and aerodynamic behavior of the turbine by conventional aerodynamic analysis methods, such as the finite volume method, due to the size and complexity inherent to this type of problem, says Loureiro [31]. For example, in wind turbines, blades can be very thin at the end, and also have a little twist to it, so that, maintaining fluid dynamic contact on the blade across of range of wind velocities and different angles of attack and different yaw is a complex fluid mechanics problem [33].

For this reason, the process of development and aerodynamic optimization is still many times conducted using analytical or semi-analytical methods, which implies the necessity for experimental or simulated data of aerodynamic properties of the airfoil profile to be employed in the construction of the turbine blades. Here is where the current methodology for wind turbine analysis encounters the greatest obstacle to its generalization to larger diameter rotors, as it begins to exceed the range of available experimental data [31]. This aspect has proved especially important for large wind turbine design ($D > 100m$),

subject of this study, whose Reynolds numbers can be greater than 10^7 [31].

4.2 The Problem of Obtaining Reynolds Experimental Data

Effects of Reynolds numbers are also known as scale effects in the aeronautics society. These effects are usually coming into picture when an aircraft has to be scaled down for wind tunnel tests. Even if the design speeds of these vehicles are kept the same in the test conditions, Reynolds numbers always differ due to the effect of scaling the geometry [34].

As seen, for wind turbines, the scale effects are also known going from small (a few hundred kilowatts) to large scales (a few megawatts). In the development of wind turbine rotors, wind tunnels are mainly used for the testing of the blade sections. Therefore, the Reynolds number effects are usually taken into account by testing the airfoils used on a blade for the proper Reynolds numbers.

However, for the Reynolds number ranges that a large 20 MW wind turbine is introducing, there is no wind tunnel data available for the wind turbine airfoils. It is also not possible to directly translate the knowledge gained from the aircrafts to the wind turbines about the Reynolds number effects, because most of the aircrafts are designed for at least the transonic wind speeds where the Mach numbers are around 0.8, in which the compressibility effects are not negligible and there is shock wave on the wing. Along a 20 MW wind turbine blade, however, the air is still below Mach number of 0.3, where it is assumed to be incompressible. A deeper study of these effects can be found in the bibliography [34].

As seen in the previous chapter, it is necessary to use the polar curves of the airfoil profiles in order to obtain the optimum values for the chord c and for the twist β of each element of the blade, and also to determine the real efficiency and the corresponding applied forces obtained by the BEM Theory. The polar curves of a given airfoil profile, in its turn, depend on the Reynolds number, which is function of W and c, variables to be determined, as shown in Eq. (3.28).

The methodology generally accepted to bypass this difficulty is the use of polar curves corresponding to an estimated Reynolds number, with the need of a re-design after the calculation of the induction factors by the BEM method if a very different Reynolds number from the estimated value is obtained, since this can lead to a large uncertainty in the results.

Considering this, Loureiro [31], during his internship at the laboratory GRANTE, developed a procedure that consists in determining the local Reynolds number in each blade element through an iterative process and without the use of experimental data.

4.3 A Procedure for Determining Reynolds for Large Wind Turbines

The polar curves corresponding to a given Reynolds number are obtained numerically, by resorting to the incorporation of XFOIL, an airfoil design and analysis open source code [35]. This code uses the method of the panels and the viscous formulation for the two-dimensional calculation of the flow around an airfoil profile, which is defined by points in a normalized form. Moreover, it enables the calculation of the aerodynamic coefficients C_l, C_d and C_m for a given Reynolds number and angle of attack α, and the generation in real-time of the necessary polar curves.

In the calculation of each blade element, after an initial estimation of the Reynolds number, appropriate to the diameter of the turbine, the polar curves can be obtained for this value, which allows one to calculate the ideal chord c or the induction factors a and a', and the incident flow velocity W. Finally, a new estimate for Re can be made, repeating the process until a convergence is achieved.

This method therefore involves providing a wind speed U for the calculation of W, even in the case of determining the optimum geometry, which, according to the theoretical model, should be independent of this parameter, since the equations for the design are obtained considering variable rotation speed and maximum efficiency. Thus, the actual effect of U on the ideal design for variable rotation speed must be examined.

This examination is done by Loureiro [31] in his report, where he concludes that the effect of the wind speed U on the optimal geometry effect is significant, causing an average variation of approximately 0.2 degrees on the twist β and 0.08 meters on the chord α for every variation of 1 m/s of the wind speed. He also concludes that considering an exact Reynolds number for obtaining the ideal geometry may lead to a better aerodynamic optimization, where, even when one designs the turbine for an operating mode with a variable rotational speed, the wind speed must be considered.

This procedure, besides leading to an initial project possibly closer to the optimum, eliminates the dependence on experimental data [31]. On the other hand, the calculation of each polar curve by XFOIL is, in its turn, also an iterative process, which results in greater computational cost and lower robustness of the method, in addition to an unknown accuracy for such calculations due to the lack of experimental data.

This iterative cycle is applied around the calculation of the ideal and the real blade element. The calculation of the real element, as described by the BEM Theory, is also an iterative calculation, thus becoming evident the high computational cost of this approach. However, it was found that this aspect is not preponderant considering the currently available computational resources [31].

Once this procedure is implemented for the calculation of Re, it could be also introduced the calculation of the Mach number, that depends only on the flow velocity and will also have influence on the polar curves, for measuring the effects of the compressibility of air. Nevertheless, since the case study (See section 4.4.1 and chapter 7) conducted for this dissertation uses a free stream wind speed of $U = 9{,}5\ m/s$, a tip speed ratio $\lambda = 8{,}5$ and a blade length of $R = 126\ m$, it is assumed that the compressibility effects are small since the flow velocity is relatively small. From Eq. (3.20):

$$\lambda = \frac{\Omega R}{U} \quad \rightarrow \quad \Omega = \frac{\lambda U}{R} = \frac{8.5 \times 9.5}{126} = 0.641\ rad/s$$

$$Mach = \frac{\Omega R}{v_s} = \frac{0.641 \times 126}{340} = \frac{80.766}{340} = 0.2375$$

Where v_s is the speed of sound. Thus, one considers here a fixed Mach number of 0.2.

4.4 Model Implementation

4.4.1 Design Parameters

The turbine is dimensioned having as initial parameters: the radius R, the number of blades B and the tip speed ratio λ. The radius R must be dimensioned considering the desired power P for a given wind speed U and considering an estimation of the turbine total efficiency Ϙ. The relation among these parameters is given as

$$P = \text{Ϙ} C_P \frac{1}{2} \rho \pi R^2 U^3 \tag{4.1}$$

Although the wind speed U is determinant for the calculation of the generated power and the forces acting on the blade, the procedure of aerodynamic optimization is conducted considering a turbine with a variable rotation speed Ω in function of U, that is, with a constant tip speed ratio λ.

$$\Omega = \frac{\lambda U}{R} \tag{4.2}$$

Thus, as seen in the theoretical model, the aerodynamic dimensioning and the corresponding efficiency C_P are functions of λ, but less dependant of U, allowing the turbine to work on maximum efficiency at different wind speeds [31]. On the other hand, the imposition of a maximum value of Ω, limited by structural issues, implies the reduction of λ relative to the value established for the design, which will contribute to a loss of efficiency

when the wind speed is too high. Moreover, the energy generation is also limited by the capacity of the generator, resulting in a power curve plateau.

Finally, an additional parameter μ_c is given by the turbine hub diameter, which determines the loss factor at the root.

4.4.2 Algorithm of the Adopted Procedure

Based on the design parameters defined in the previous section (B, R, λ, U e μ_c), the large wind turbine design is carried out by the following steps, which are also outlined in the diagram of Figure 4.1.

1. The ideal parameters c and β are calculated for each blade element dr, in function of its position along the span $\mu = r/R$ (according to the Section *Ideal Element*).
   The type of airfoil profile enters as an additional parameter, and can be selected according to the calculated local efficiency dC_P or geometric characteristics such as the airfoil profile thickness, or be generated by interpolation between the neighboring profiles. If one chooses a calculated criterion, the choice must be made using the step 2 iteratively, although the most usual case is the use of a previously known airfoil profile distribution, based on the required profile thickness to meet requirements at the structural level;

2. The real aerodynamics parameters are calculated, including the local efficiency and the applied forces (according to the Section *Blade Element Momentum Theory*), and the geometric properties of the cross-section of the airfoil profile;

3. After repeating the previous steps for each blade element independently, the turbine global parameters, such as the efficiency C_P, the thrust T and the torque Q, are calculated by integration of the local values along the blade;
   Simultaneously, the internal forces (shear forces and bending and torsional moments) and the stress distribution are calculated.

Optionally:

4. Introduce necessary modifications on the chord c and on the twist angle β to meet other design requirements or to smooth discontinuities caused by the transition between different types of airfoil profile, and repeat steps 2 and 3. This step 4 implies a loss of aerodynamic efficiency;

5. Simulate non-optimal operating conditions by the introduction of variations to the turbine design parameters, such as λ, U or β_o, and repeat steps 2 and 3 in order to examine the effect of these variations on the global results of the turbine.

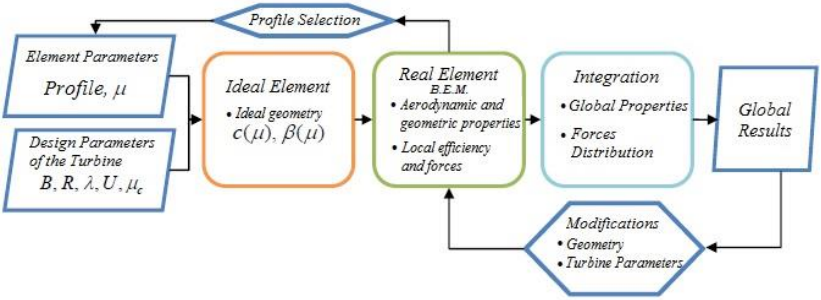

Figure 4.1 – The general procedure flow diagram for the turbine design [31].

For the calculation of the ideal blade element, the model contains more approximations and, for the real blade element, non-optimal working conditions can be introduced.

The implementation of these calculations follows, in general, the analytical model presented in the previous chapter, with the introduction of two additional procedures: i) The convergence of the Reynolds number, presented in the previous section, and ii) The correction of the chord c by the Prandtl loss factor, as follows:

$$c = F\frac{8\pi\mu R}{BC_l}(1-\cos\phi) \qquad (3.57)^*$$

A more thorough discussion about the correction of the chord and about the convergence of the calculations can be found in the report written by Loureiro [31].

The method used for obtaining the ideal geometry and the parameters of the blade element, with the calculation of the Reynolds number and the chord correction, is schematized in the following flow diagram:

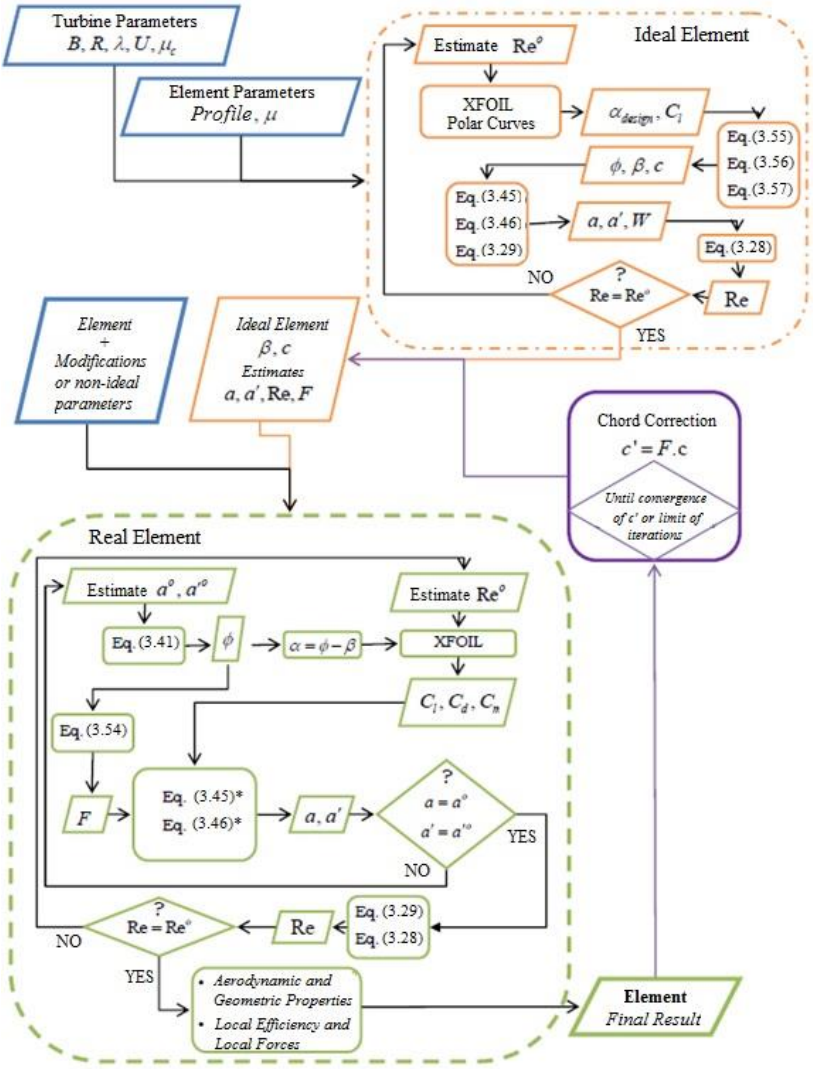

Figure 4.2 – Flow diagram for the calculation of a blade element [31].

4.4.3 Integration of the Global Results

After describing how to obtain the results for each blade element, one now must obtain the global results for the large wind turbine.

The theoretical model of the blade element defines the aerodynamic forces and efficiency for an element of length dr. However, due to the uncertainty regarding the convergence of the numerical calculation of these results, the number of blade elements and their respective length dr are not known at the start. Therefore, the results obtained for the elements are calculated per unit length, and this length is only defined in the calculation of the global results by numerical integration [31].

The numerical integration of a generic variable φ is made using the trapezoidal rule, as shown in equation (4.3), where $\frac{d\varphi}{dr}$ can correspond to $\frac{dC_P}{dr}$, $\frac{dT}{dr}$ or $\frac{dQ}{dr}$.

$$\varphi = \int_{r_c}^{R} \frac{d\varphi}{dr} dr \approx \sum_{i=1}^{N-1} (\mu_{i+1} - \mu_i) \left[\left(\frac{d\varphi}{dr} \right)_i + \left(\frac{d\varphi}{dr} \right)_{i+1} \right] \frac{R}{2} \tag{4.3}$$

With N being the number of blade elements.

Bearing in mind the concavity of the curves of dC_P, dT and dQ in function of μ, the trapezoid method will tend to underestimate the integral values, but the error must be smaller than that which would be obtained using a midpoint rule, given the variability in distance between the points calculated [31].

CHAPTER 5

SHELL THEORIES APPLIED ON THIN-WALLED MULTILAYER BLADES

This chapter discusses multilayer shell theories and the relationship between the internal forces and the corresponding deformations on a thin-walled blade. It begins with a brief introduction of the stress/strain relationship in the orthotropic axis of a generic layer *k* and further the stress/strain relationship in the local axis of an infinitesimal multilayer blade element. Then, the nomenclature of the normal and shear stresses developed due to aerodynamics loads is presented (centrifugal, gravitational and gyroscopic loads are not covered in this dissertation). Finally, a brief discussion on failure criteria for composite materials ends the chapter.

5.1 Stress/Strain Relationship in the Orthotropic Axis (1, 2, 3)

An infinitesimal element of the layer k^{th} is defined with dimensions ds_1 and ds_2 in the plane of the layer and with a thickness h_k. The fiber direction in the layer defines the directions of the orthotropic axes. As shown below in Figure 5.1, direction 1 is parallel to the fiber and direction 2 is orthogonal to the fiber in the plane of the layer. Thus, direction 3 is normal to the plane of the layer.

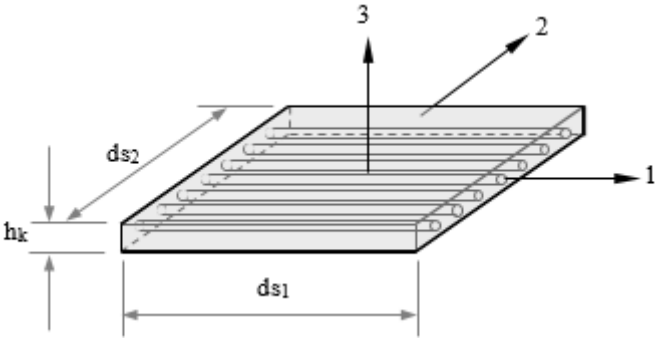

Figure 5.1 – Infinitesimal element of the k^{th} layer in the orthotropic axis.

As shown by Reddy [36], the stress/strain relationship in the orthotropic axis is given as

$$\begin{Bmatrix} \sigma_1 \\ \sigma_2 \\ \sigma_3 \\ \tau_{23} \\ \tau_{13} \\ \tau_{12} \end{Bmatrix} = \begin{bmatrix} Q_{11} & Q_{12} & Q_{13} & 0 & 0 & 0 \\ Q_{21} & Q_{22} & Q_{23} & 0 & 0 & 0 \\ Q_{31} & Q_{32} & Q_{33} & 0 & 0 & 0 \\ 0 & 0 & 0 & Q_{44} & 0 & 0 \\ 0 & 0 & 0 & 0 & Q_{55} & 0 \\ 0 & 0 & 0 & 0 & 0 & Q_{66} \end{bmatrix} \begin{Bmatrix} \varepsilon_1 \\ \varepsilon_2 \\ \varepsilon_3 \\ \gamma_{23} \\ \gamma_{13} \\ \gamma_{12} \end{Bmatrix} \tag{5.1}$$

The terms in the symmetric constitutive matrix are

$$\begin{aligned} Q_{11} &= E_1 \frac{1-\nu_{23}\nu_{32}}{\Delta}; \quad Q_{12} = E_1 \frac{\nu_{21}+\nu_{31}\nu_{23}}{\Delta}; \quad Q_{44} = G_{23} \\ Q_{22} &= E_2 \frac{1-\nu_{13}\nu_{31}}{\Delta}; \quad Q_{13} = E_1 \frac{\nu_{31}+\nu_{21}\nu_{32}}{\Delta}; \quad Q_{55} = G_{13} \\ Q_{33} &= E_3 \frac{1-\nu_{12}\nu_{21}}{\Delta}; \quad Q_{23} = E_2 \frac{\nu_{32}+\nu_{12}\nu_{31}}{\Delta}; \quad Q_{66} = G_{12} \end{aligned} \tag{5.2}$$

With

$$\Delta = 1 - \nu_{12}\nu_{21} - \nu_{23}\nu_{32} - \nu_{13}\nu_{31} - 2\nu_{21}\nu_{32}\nu_{13} \tag{5.3}$$

Considering the in-plane stress state, Eq. (5.1) can be reduced to

$$\begin{Bmatrix} \sigma_1 \\ \sigma_2 \\ \tau_{12} \end{Bmatrix} = \begin{bmatrix} Q_{11} & Q_{12} & 0 \\ Q_{21} & Q_{22} & 0 \\ 0 & 0 & Q_{66} \end{bmatrix} \begin{Bmatrix} \varepsilon_1 \\ \varepsilon_2 \\ \gamma_{12} \end{Bmatrix} \tag{5.4}$$

And the transversal shear stresses are

$$\begin{Bmatrix} \tau_{13} \\ \tau_{23} \end{Bmatrix} = \begin{bmatrix} Q_{44} & 0 \\ 0 & Q_{55} \end{bmatrix} \begin{Bmatrix} \gamma_{13} \\ \gamma_{23} \end{Bmatrix} \tag{5.5}$$

Where now

$$\begin{gathered} Q_{11} = {E_1}/{(1 - \nu_{12}\nu_{21})} \\ Q_{22} = {E_2}/{(1 - \nu_{12}\nu_{21})} \\ Q_{12} = Q_{21} = {\nu_{21}E_1}/{(1 - \nu_{12}\nu_{21})} \\ Q_{44} = G_{23}; \quad Q_{55} = G_{31}; \quad Q_{66} = G_{12} \end{gathered} \tag{5.6}$$

5.2 Stress/Strain Relationship in the Local Axis (x, y, z)

A multilayer composite blade is built with a number n of layers, where each layer has a thickness h_k and a fiber direction θ_k with respect to the direction x of the local axis (x, y, z), as shown in Figure 5.2.

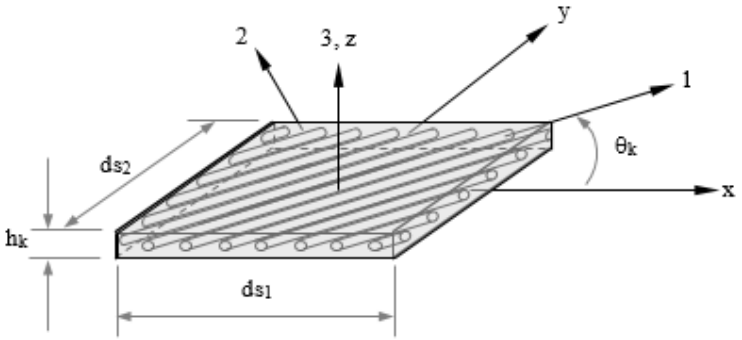

Figure 5.2 – Infinitesimal element of a layer *k* in the orthotropic axis and local axis.

Applying the coordinate transformation rule to Eq. (5.1), the in-plane stress/strain relationship in the local coordinate axis is given as

$$\begin{Bmatrix}\sigma_x\\ \sigma_y\\ \tau_{xy}\end{Bmatrix}_k = \begin{bmatrix}\bar{Q}_{11} & \bar{Q}_{12} & \bar{Q}_{16}\\ \bar{Q}_{21} & \bar{Q}_{22} & \bar{Q}_{26}\\ \bar{Q}_{61} & \bar{Q}_{62} & \bar{Q}_{66}\end{bmatrix}_k \begin{Bmatrix}\varepsilon_x\\ \varepsilon_y\\ \gamma_{xy}\end{Bmatrix}_k \tag{5.7}$$

Where the terms of the symmetric constitutive matrix are [36]

$$\begin{aligned}
\bar{Q}_{11} &= c^4Q_{11} + s^4Q_{22} + 2c^2s^2(Q_{12} + 2Q_{66})\\
\bar{Q}_{22} &= s^4Q_{11} + c^4Q_{22} + 2c^2s^2(Q_{12} + 2Q_{66})\\
\bar{Q}_{66} &= c^2s^2(Q_{11} + Q_{22} - 2Q_{12} - 2Q_{66}) + (c^4 + s^4)Q_{66}\\
\bar{Q}_{12} &= \bar{Q}_{21} = c^2s^2(Q_{11} + Q_{22} - 4Q_{66}) + (c^4 + s^4)Q_{12}\\
\bar{Q}_{16} &= \bar{Q}_{61} = (Q_{11} - Q_{12} - 2Q_{66})c^3s + (2Q_{66} + Q_{12} - Q_{22})cs^3\\
\bar{Q}_{26} &= \bar{Q}_{62} = (Q_{12} - Q_{22} + 2Q_{66})c^3s + (Q_{11} - Q_{12} - 2Q_{66})cs^3\\
s &= \sin\theta_k;\ \ c = cos\theta_k
\end{aligned} \tag{5.8}$$

The relationship between the in-plane stress in the orthotropic axis and the in-plane stress in the local axis is given as

$$\begin{Bmatrix} \sigma_x \\ \sigma_y \\ \tau_{xy} \end{Bmatrix}_k = \begin{bmatrix} c^2 & s^2 & -2cs \\ s^2 & c^2 & 2cs \\ cs & -cs & c^2 - s^2 \end{bmatrix}_k \begin{Bmatrix} \sigma_1 \\ \sigma_2 \\ \tau_{12} \end{Bmatrix}_k \tag{5.9}$$

And applying the coordinate transformation rule to Eq. (5.5), the transversal shear stress/shear strain relationship in the local coordinate axis is given as

$$\begin{Bmatrix} \tau_{yz} \\ \tau_{xz} \end{Bmatrix}_k = \begin{bmatrix} \bar{Q}_{44} & \bar{Q}_{45} \\ \bar{Q}_{54} & \bar{Q}_{55} \end{bmatrix}_k \begin{Bmatrix} \gamma_{yz} \\ \gamma_{xz} \end{Bmatrix}_k \tag{5.10}$$

Where [36]

$$\begin{aligned} \bar{Q}_{44} &= Q_{44}c^2 + Q_{55}s^2 \\ \bar{Q}_{45} &= (Q_{55} - Q_{44})cs \\ \bar{Q}_{55} &= Q_{55}c^2 + Q_{44}s^2 \end{aligned} \tag{5.11}$$

The relationship between transversal shear stress in the orthotropic axis and in the local axis is given as

$$\begin{Bmatrix} \tau_{yz} \\ \tau_{xz} \end{Bmatrix}_k = \begin{bmatrix} c & s \\ s & c \end{bmatrix}_k \begin{Bmatrix} \tau_{23} \\ \tau_{13} \end{Bmatrix}_k \tag{5.12}$$

5.3 Strain State of a Multilayer Plate by the First Order Theory

The stress state on multilayer shell structures can be obtained by using different theories depending on the small or large strain level they will be submitted throughout the loading. In the present work, it is assumed that there are no large deformations nor warping of the cross section of the blade.

The strain state is defined by the First Order Theory, which includes the transversal shear deformation. For a thin-walled blade, the normal strain in the direction z of the local axis is neglected. Thus the strain state is as shown below

$$\varepsilon_x = \frac{\partial u_0}{\partial x} + z\frac{\partial \alpha}{\partial x}$$

$$\varepsilon_y = \frac{\partial v_0}{\partial y} + z\frac{\partial \beta}{\partial y}$$

$$\gamma_{xy} = \left(\frac{\partial u_0}{\partial y} + \frac{\partial v_0}{\partial x}\right) + z\left(\frac{\partial \alpha}{\partial y} + \frac{\partial \beta}{\partial x}\right) \tag{5.11}$$

$$\gamma_{yz} = \frac{\partial v}{\partial z} + \frac{\partial w}{\partial y}$$

$$\gamma_{xz} = \frac{\partial u}{\partial z} + \frac{\partial w}{\partial x}$$

The reduced form of the strain state is given as follows

$$\varepsilon_x = \varepsilon_x^0 + z\kappa_x$$

$$\varepsilon_y = \varepsilon_y^0 + z\kappa_y \tag{5.12}$$

$$\gamma_{xy} = \gamma_{xy}^0 + z\kappa_{xy}$$

$$\gamma_{yz} = \beta + \frac{\partial w_0}{\partial y}$$

$$\gamma_{xz} = \alpha + \frac{\partial w_0}{\partial x}$$

Where $\varepsilon_x^0, \varepsilon_y^0$ e γ_{xy}^0 are the normal and shear strains in the neutral surface, κ_x, κ_y e κ_{xy} are the curvatures, α and β are the rotation of the cross section around directions y and x, respectively, and z is the position where the strain is determined [36].

5.4 Stress Nomenclature on a Multilayer Composite Blade

This section presents the nomenclature of the stresses developed in the multilayer composite blade that will be used throughout this dissertation. As seen earlier, the internal forces developed in the blade due to the aerodynamic loads are the bending moments M_t and M_a, the torsional moment M_r, and the shear forces Q_t and Q_a developed in the tangential and axial directions of the blade, t and a, respectivelly. In the figures 5.3 and 5.4, one can see these internal forces and the stresses developed in a generic multilayer infinitesimal element.

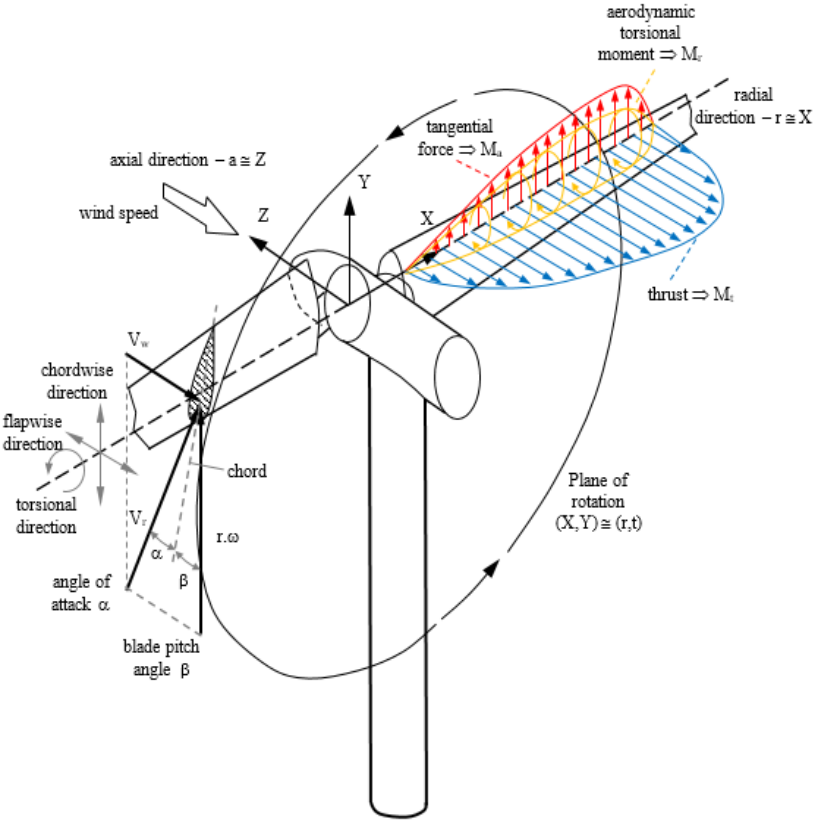

Figure 5.3 – Schematic of a conventional wind turbine and the aerodynamic loads acting on it. (Source: Hau [32])

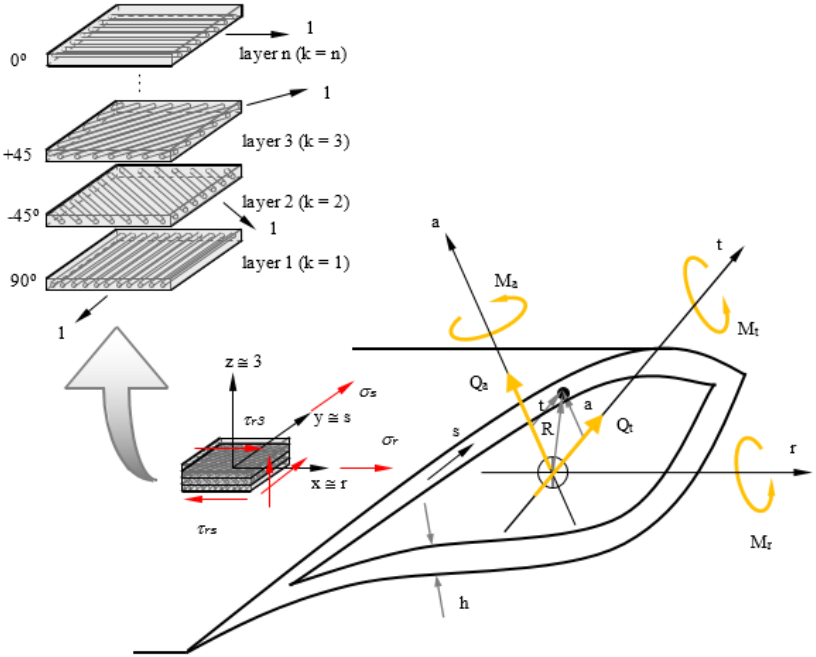

Figure 5.4 – Stress state on a thin-walled composite blade.

Direction s goes along the perimeter direction of the blade. The local coordinate system of the infinitesimal multilayer element is (x, y, z). Thus, locally, the direction x is coincident with the wingspan direction, r, direction y is coincident with the perimeter direction, s, and direction z is coincident with the normal direction to the plane of the layers, 3. Based on these directions, the stresses developed in a thin-walled blade are

- σ_r – normal stress in the wingspan direction, r, due to bending moments M_a and M_t;
- σ_s – normal stress in the perimeter direction, s;
- τ_{rs} – plane shear stress due to torsional moment M_r;

- τ_{r3} – transversal shear stress due to shear forces Q_t and Q_a;

These developed normal and shear stresses can be calculated after the determination of the curvatures and transverse shear strains that are related to the aerodynamic forces. These curvatures and transverse shear strains are as follows

- κ_{r-t} – curvature on the plane (r, t), due to bending moment M_t;
- κ_{r-a} – curvature on the plane (r, a), due to bending moment M_a;
- κ_{rs} – curvature due to torsional moment M_r;
- γ_{rt} – transversal shear strain due to shear force Q_t;
- γ_{ra} – transversal shear strain due to shear force Q_a.

The in-plane stress/strain relationship in the local axis of a point with coordinates (t, a) in the k^{th} layer, as shown in Figure 5.3, is given as follows

$$\begin{Bmatrix} \sigma_r \\ \sigma_s \\ \tau_{rs} \end{Bmatrix}_k = \begin{bmatrix} \bar{Q}_{11} & \bar{Q}_{12} & \bar{Q}_{16} \\ \bar{Q}_{21} & \bar{Q}_{22} & \bar{Q}_{26} \\ \bar{Q}_{61} & \bar{Q}_{62} & \bar{Q}_{66} \end{bmatrix}_k \begin{Bmatrix} \varepsilon_r \\ \varepsilon_s \\ \gamma_{rs} \end{Bmatrix} \tag{5.13}$$

For large wind turbine, the blade is assumed to be a long and slender beam. Thus, classical assumptions concerning bending and torsion of beams are valid. So, the normal stress and the linear deformation in the perimeter direction are supposed null, $\sigma_s = 0$ and $\varepsilon_s = 0$.

Thus, if the linear deformation and the shear deformation are due to bending and torsional moments, the in-plane stress/strain relationship in the local axis of a point with coordinates (t, a) in the Equation (5.14) can be written as

$$\begin{Bmatrix} \sigma_r \\ 0 \\ \tau_{rs} \end{Bmatrix}_k = \begin{bmatrix} \bar{Q}_{11} & \bar{Q}_{12} & \bar{Q}_{16} \\ \bar{Q}_{21} & \bar{Q}_{22} & \bar{Q}_{26} \\ \bar{Q}_{61} & \bar{Q}_{62} & \bar{Q}_{66} \end{bmatrix}_k \begin{Bmatrix} (a.\kappa_{r-t} + t.\kappa_{r-a}) \\ 0 \\ R.\kappa_{rs} \end{Bmatrix} \quad (5.14)$$

And the transversal shear stress/shear strain relationship in the local coordinate axis is given as

$$\{\tau_{r3}\}_k = [\bar{Q}_{55}]_k \{\gamma_{r3}\} \quad (5.15)$$

5.5 Lamina Strength

Failure criteria are designed to allow the designer to evaluate the mechanical strength of laminated structures. The rupture of composite material laminated structures can occur through different mechanisms: fiber rupture, matrix rupture, fiber/matrix decohesion, delamination (detachment of the blades), etc.

The failure criteria can be classified as:

- Maximum Stress Criterion,
- Maximum Strain Criterion,
- Interactive or Energy Criteria.

The Maximum Stress Criterion stipulates that the mechanical strength of the analyzed lamina is reached when one of the three stresses to which the lamina is being subjected, reaches the value of the corresponding rupture stress.

The Maximum Strain Criterion, in its turn, stipulates that the mechanical strength of the analyzed lamina is reached when one of the three strains to which the blade is being subjected, reaches the value of the corresponding rupture strain.

For the Maximum Stress and Maximum Strain criteria, it is assumed that the mechanisms for longitudinal, transverse and shear rupture occur independently. In order to take all these mechanisms into account

simultaneously, as in the von Mises criterion for isotropic materials, the interactive or energy criteria were developed.

Although several energy failure criteria for composite materials have been developed and presented in the literature, such as Hill, Hoffman, Tsai-Hill, Tsai-Wu criterion and so on, only the last one will be briefly discussed in this section, since this is the one implemented in the code developed in this work.

The Tsai-Wu criterion was developed in order to improve the correlation between experimental and theoretical results through the introduction of additional parameters. It is one of several quadratic interaction failure criteria found in the literature [37] and is expressed by Equation (5.16) when the orthotropic composite material is subjected to an in-plane stress state

$$\frac{\sigma_1^2}{X_1^T X_1^C} + \frac{\sigma_2^2}{X_2^T X_2^C} + \left(\frac{1}{X_1^T} - \frac{1}{X_1^C}\right)\sigma_1 + \left(\frac{1}{X_2^T} - \frac{1}{X_2^C}\right)\sigma_2 + 2F_{12}\frac{\sigma_1\sigma_2}{X_1^T X_1^C} + \left(\frac{\tau_{12}}{s_{12}}\right)^2 = 1 \tag{5.16}$$

Where the in-plane stresses σ_1, σ_2 and τ_{12} are acting in the k^{th} layer and F_{12} is a coupling coefficient usually used to adjust to the results obtained experimentally, expressed as

$$F_{12} = \frac{1}{2\sigma^2}\left\{1 - \left[X_1^C - X_1^T + \frac{X_1^T X_1^C}{X_2^T X_2^C}(X_2^C - X_2^T)\right]\sigma + \left(1 + \frac{X_1^T X_1^C}{X_2^T X_2^C}\right)\sigma^2\right\} \tag{5.17}$$

or:

$$F_{12} = \frac{2}{\sigma_{45}^2}\left\{1 - \left[X_1^C - X_1^T + \frac{X_1^T X_1^C}{X_2^T X_2^C}(X_2^C - X_2^T)\right]\frac{\sigma_{45}}{2} + \left(1 + \frac{X_1^T X_1^C}{X_2^T X_2^C} + \frac{X_1^T X_1^C}{S_{12_C}}\right)\frac{\sigma_{45}^2}{2}\right\} \tag{5.18}$$

and may vary from

$$-1 \leq F_{12} \leq 1 \tag{5.19}$$

σ and σ_{45} are the rupture stresses determined respectively in biaxial tests (σ) and tensile tests at 45º (σ_{45}). The ultimate strengths are defined as

- X_1^T – tensile strength in fiber direction (1);
- X_1^C – compressive strength in fiber direction (1);
- X_2^T – tensile strength in transverse direction (2);
- X_2^C – compressive strength in transverse direction (2);
- S_{12} – shear strength in the plane (1-2);

For the transversal shear stresses, the Maximum Stress Criterion can be applied and is expressed by

$$\frac{\tau_{13}}{S_{13}} = 1 \qquad \frac{\tau_{23}}{S_{23}} = 1 \tag{5.20}$$

Where the transversal shear stresses τ_{13} and τ_{23} are acting in the k^{th} layer and the ultimate strengths are defined as follows

- S_{13} – shear strength in the transverse plane (1-3);

- S_{23} – shear strength in the transverse plane (2-3);

It is worth noting that, by making $F_{12} = -1/2$, Tsai-Wu criterion becomes Hoffmann criterion. Further, by making $X_1^T = X_1^C = X_1$ and $X_2^T = X_2^C = X_2$, the criterion transforms into Tsai-Hill.

5.6 Concluding Remarks

This chapter has introduced the multilayer shell theories and the relationship between the internal forces due to aerodynamics loads presented earlier in the chapter and the corresponding deformations on a thin-walled blade. Even though the aerodynamic loads correspond to bending moments M_a and M_t, torsional moment M_r and shear forces Q_a and Q_t, that generate in-plane stress and transversal shear stress, this latter stress is not in the scope of this work.

CHAPTER 6

THE SHEAR FLOW THEORY FOR STRESS ANALYSIS ON THIN-WALLED MULTILAYER BLADES

This chapter discusses the development and implementation of the Shear Flow Theory for determining the in-plane stresses developed on a wind turbine blade due to the aerodynamic loads. The normal and shear stresses on the plane of the blade are determined by imposing the equilibrium on bending and torsional moments. The theory for multilayer shells seen in the Chapter 5 is applied. The transverse shear stresses determination is not part of the scope of the present work.

6.1 Introduction

As mentioned in the previous chapter, the blade of a large horizontal axis wind turbine, object of this research, is a thin-walled composite shell. The next sections in this chapter describe the development employed in order to determine the in-plane stresses for further failure criteria application on composite materials.

6.2 In-Plane Stresses on Multilayer Composite Blades

In Figure 6.1, are shown the in-plane stresses on a multilayer composite blade developed due to aerodynamic bending moments M_t and M_a and aerodynamic torsional moment M_r.

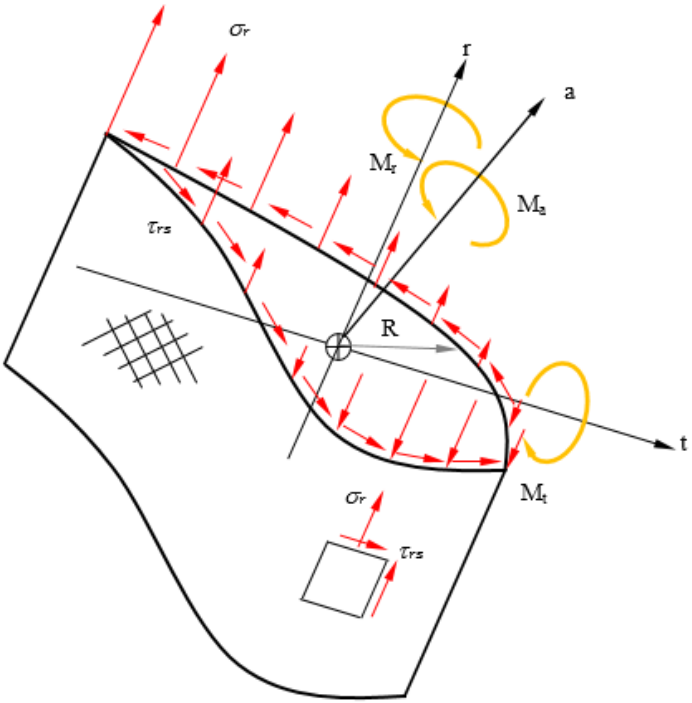

Figure 6.1 – In-plane stress state on a multilayer composite blade.

From Figure 6.2, the relationship between bending and torsional moments with normal and shear stresses on the plane of the blade is obtained by the equilibrium equations as

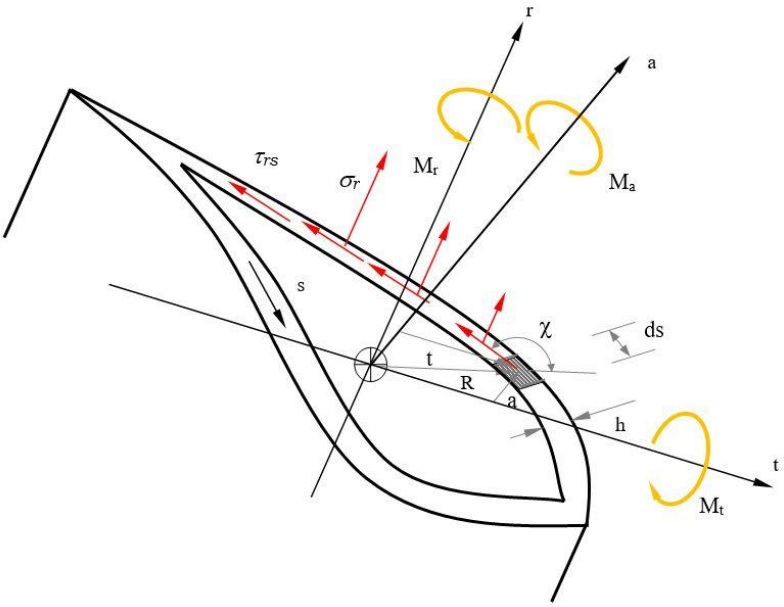

Figure 6.2 – In-plane stress and aerodynamic internal moments relationship.

$$M_t = \oint \int_{-h/2}^{h/2} (\sigma_{r-t}\, dh\, ds)\, a$$

$$M_a = \oint \int_{-h/2}^{h/2} (\sigma_{r-a}\, dh\, ds)\, t \qquad (6.1)$$

$$M_r = \oint \int_{-h/2}^{h/2} (\tau_{rs}\, dh\, ds)\, R\, \sin\chi$$

where ds is the length of an infinitesimal element of shell, dh is the infinitesimal thickness of a layer k, a is the distance between the centroid of the infinitesimal area and the transversal axis, t is the distance between

the centroid of the infinitesimal area and the axial axis, R is the distance between the centroid of the infinitesimal area and the radial axis and χ is the angle between the vector R and the vector τ_{rs}.

The normal stresses σ_{r-t} and σ_{r-a} are related as

$$\sigma_r = \sigma_{r-t} + \sigma_{r-a} \tag{6.2}$$

The first integral in Equation (6.1) is a line integral that is performed along the perimeter of the blade cross section, or in the s direction. The second integral is performed along the total thickness of the blade. This last integral can be substituted by a sum of integrals along individual layers, resulting on the thickness h_k of each individual layer. The total number of layers is N. Therefore:

$$\begin{aligned} M_t &= \sum_{k=1}^{N} \oint \sigma_{r-t}\, h_k\, a\, ds \\ M_a &= \sum_{k=1}^{N} \oint \sigma_{r-a}\, h_k\, t\, ds \\ M_r &= \sum_{k=1}^{N} \oint \tau_{rs}\, h_k\, R\, \sin\chi\, ds \end{aligned} \tag{6.3}$$

Substituting Eq. (5.14) in Chapter 5 into Eq. (6.3) and developing, it follows that

$$M_t = \sum_{k=1}^{N} \oint \left(\bar{Q}_{11}^{k}\, a\, \kappa_{r-t} + \bar{Q}_{16}^{k} R\, \kappa_{rs} \right) h_k\, a\, ds \tag{6.4}$$

$$M_a = \sum_{k=1}^{N} \oint \left(\bar{Q}_{11}^k \, t \, \kappa_{r-a} + \bar{Q}_{16}^k R \, \kappa_{rs} \right) h_k \, t \, ds$$

$$M_r = \sum_{k=1}^{N} \oint [\bar{Q}_{61}^k \, (a \, \kappa_{r-t} + t \, \kappa_{r-a}) + \bar{Q}_{66}^k \, R \, \kappa_{rs}] \, h_k \, R \, \sin\chi \, ds$$

For any section with a path s that defines the perimeter of the airfoil and the relationship with its coordinates (t, a), the line integral can be performed. Thus, the curvatures κ_{r-t}, κ_{r-a}, and κ_{rs} can be determined as a function of the aerodynamic bending and torsional moments.

6.3 The Shear Flow Theory on a Discrete Multilayer Profile

If a cross section of the airfoil profile is discretized on M cells, Eq. (6.4) can be rewritten as follows

$$M_t = \sum_{k=1}^{N} \sum_{i}^{M} \left(\bar{Q}_{11}^k a \, \kappa_{r-t} + \bar{Q}_{16}^k R \, \kappa_{rs} \right) h_k \, a \, \Delta s$$

$$M_a = \sum_{k=1}^{N} \sum_{i}^{M} \left(\bar{Q}_{11}^k \, t \, \kappa_{r-a} + \bar{Q}_{16}^k R \, \kappa_{rs} \right) h_k \, t \, \Delta s \qquad (6.5)$$

$$M_r = \sum_{k=1}^{N} \sum_{i}^{M} [\bar{Q}_{61}^k \, (a \, \kappa_{r-t} + t \, \kappa_{r-a}) + \bar{Q}_{66}^k \, R \, \kappa_{rs}] \, h_k \, R \, \sin\chi \, \Delta s$$

Where

$$a = \left(\frac{a_{i+1} + a_i}{2} \right) \qquad (6.6)$$

$$t = \left(\frac{t_{i+1} + t_i}{2}\right)$$

$$R = \sqrt{\left(\frac{a_{i+1} + a_i}{2}\right)^2 + \left(\frac{t_{i+1} + t_i}{2}\right)^2}$$

$$\Delta s = \sqrt{(a_{i+1} - a_i)^2 + (t_{i+1} - t_i)^2}$$

So, the aerodynamic moments and the curvatures can be related

$$\begin{Bmatrix} M_t \\ M_a \\ M_r \end{Bmatrix} = \begin{bmatrix} D_{11} & D_{12} & D_{16} \\ D_{21} & D_{22} & D_{26} \\ D_{61} & D_{62} & D_{66} \end{bmatrix} \begin{Bmatrix} \kappa_{r-t} \\ \kappa_{r-a} \\ \kappa_{rs} \end{Bmatrix} \tag{6.7}$$

Finally, the curvatures can be obtained as

$$\begin{Bmatrix} \kappa_{r-t} \\ \kappa_{r-a} \\ \kappa_{rs} \end{Bmatrix} = \begin{bmatrix} D_{11} & D_{12} & D_{16} \\ D_{21} & D_{22} & D_{26} \\ D_{61} & D_{62} & D_{66} \end{bmatrix}^{-1} \begin{Bmatrix} M_t \\ M_a \\ M_r \end{Bmatrix} \tag{6.8}$$

The in-plane stress distribution on each blade element can be determined on a point with coordinates (t, a) in the k^{th} layer by Eq. (5.14), which is reproduced below

$$\begin{Bmatrix} \sigma_r \\ 0 \\ \tau_{rs} \end{Bmatrix}_k = \begin{bmatrix} \bar{Q}_{11} & \bar{Q}_{12} & \bar{Q}_{16} \\ \bar{Q}_{21} & \bar{Q}_{22} & \bar{Q}_{26} \\ \bar{Q}_{61} & \bar{Q}_{62} & \bar{Q}_{66} \end{bmatrix}_k \begin{Bmatrix} (a.\kappa_{r-t} + t.\kappa_{r-a}) \\ 0 \\ R.\kappa_{rs} \end{Bmatrix} \tag{6.9}$$

6.4 Verification of the Shear Flow Theory on a Symmetric NACA0012 Airfoil

The purpose of this section is to compare the procedure for determining the in-plane stress state presented in Section 6.3 with the results obtained in the research proposed by Wang et al. [18]. In that study, the blade cross-section (airfoil profile) properties were calculated with respect to the coordinate system (x, y) placed at the centroid of the section (x_c, y_c). The chosen airfoil was the symmetric airfoil NACA0012, illustrated in Figure 6.3, whose geometric data is listed in Table 6.1 along with the material properties of an isotropic blade. The cross-section properties calculated by Wang et al. [18] are presented in Table 6.2.

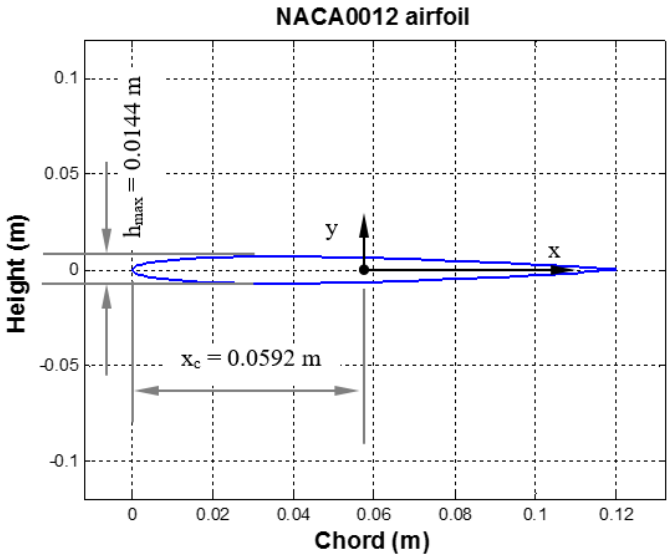

Figure 6.3 – NACA0012 airfoil schematic profile.

Table 6.1 – Geometric data and material properties of the isotropic blade cross-section.

Properties	Values
E (GPa)	210

ν	0.3
Airfoil	NACA0012
Chord c (m)	0.12
Thickness h (m)	0.000675

Table 6.2 – Calculated cross-sectional properties.

Cross-section properties	**Wang et al.**
<EA> (N)	3.4721×10^{7}
$\langle EI_x \rangle$ (Nm^2)	8.6756×10^{2}
$\langle EI_y \rangle$ (Nm^2)	4.2866×10^{4}
<GJ> (Nm^2)	1.0848×10^{3}

With the cross-sectional properties calculated in Wang et al. [18], the maximum normal and shear stresses can be calculated as it follows

$$\sigma_{z-y} = E\frac{M_x}{\langle EI_x \rangle}\frac{h_{max}}{2}$$

$$\sigma_{z-x} = E\frac{M_y}{\langle EI_y \rangle}(c - x_c) \qquad (6.10)$$

$$\tau_{x-y} = G\frac{M_z}{\langle GJ \rangle}(c - x_c)$$

For unitary bending and torsional moments $M_x = M_y = M_z = 1\ N.m$ applied individually, the maximum normal and shear stresses are

$$\sigma_{z-y} = 210.10^9 \frac{1.0}{8.6756.10^2} \frac{0.0144}{2} = 1.743\times10^6\ Pa$$

$$\sigma_{z-x} = 210.10^9 \frac{1.0}{4.2866.10^4}(0.12 - 0.0592) = 0.298\times10^6\ Pa \quad (6.11)$$

$$\tau_{x-y} = \frac{210.10^9}{2.(1+0.3)} \frac{1.0}{1.0848.10^3}(0.12 - 0.0592) = 4.527\times10^6\ Pa$$

Figure 6.4 shows the results for the in-plane stress state using the procedure presented earlier in Section 6.3 for an angle of attack $\alpha = 0°$. As it can be observed, the maximum normal and shear stresses calculated with the use of the cross-sectional properties obtained by Wang et. al [18] are fairly close to the ones obtained with the presented methodology, as it can be seen in Figure 6.4. This is also confirmed when the angle of attack is changed to $\alpha = 90°$, as shown in Figure 6.5.

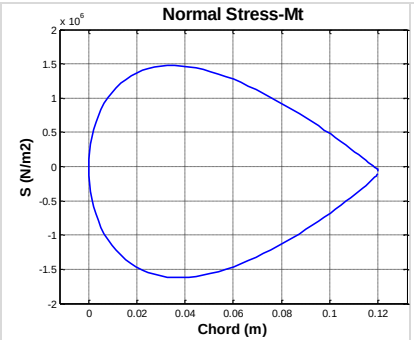

(a) (b)

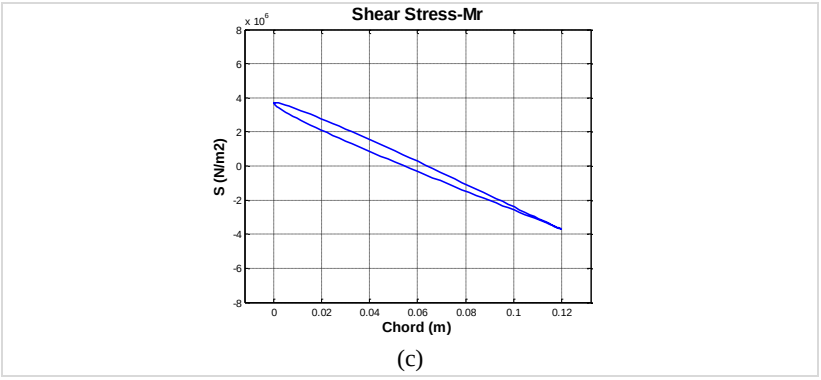

(c)

Figure 6.4 – NACA0012 airfoil in-plane stress for angle of attack α = 0°.

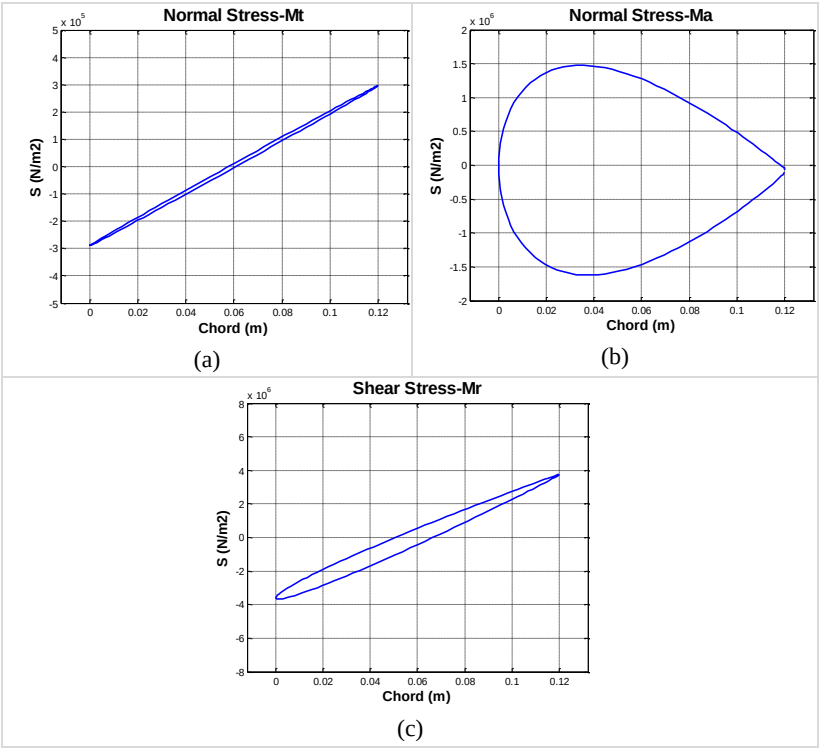

(a) (b)

(c)

Figure 6.5 – NACA0012 airfoil in-plane stress for angle of attack α = 90°.

6.5 Results of the Shear Flow Theory for an Asymmetric NACA2412 Airfoil

The purpose of this section is to apply the procedure for determining the in-plane stress state presented in Section 6.3 now for an asymmetric airfoil NACA2412, illustrated in Figure 6.6.

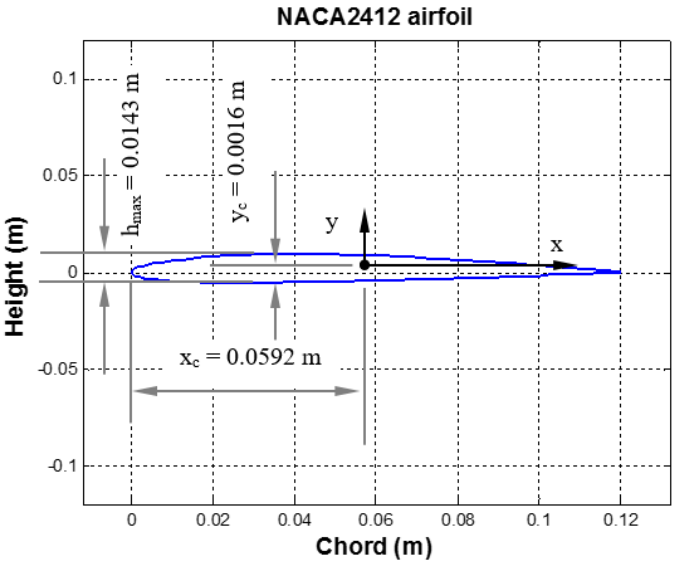

Figure 6.6 – NACA2412 airfoil schematic profile.

Figure 6.7 shows the results for the in-plane stress state using the procedure presented in Section 6.3, for an angle of attack $\alpha = 0°$. As it can be seen in Figure 6.8, the same pattern is reproduced in Figure 6.8 when the angle of attack is changed to $\alpha = 90°$.

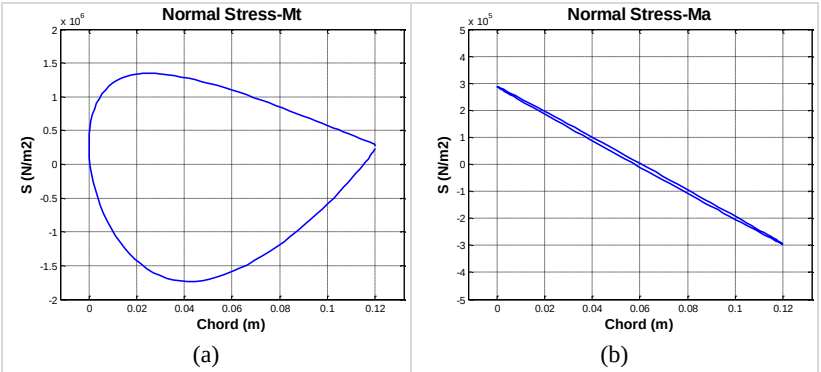

Figure 6.7 – NACA2412 airfoil in-plane stress for angle of attack α = 0°.

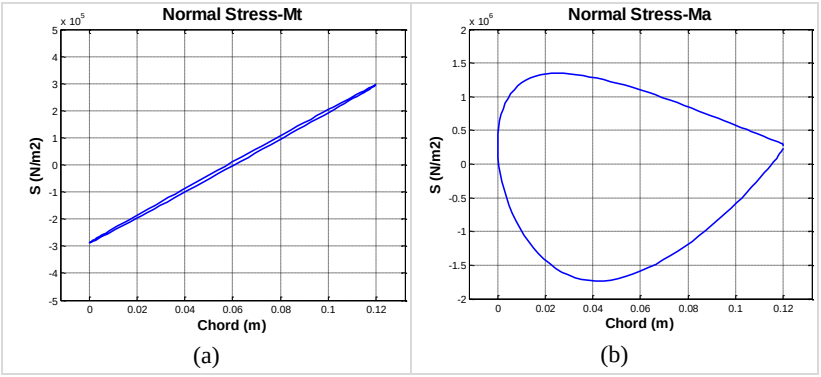

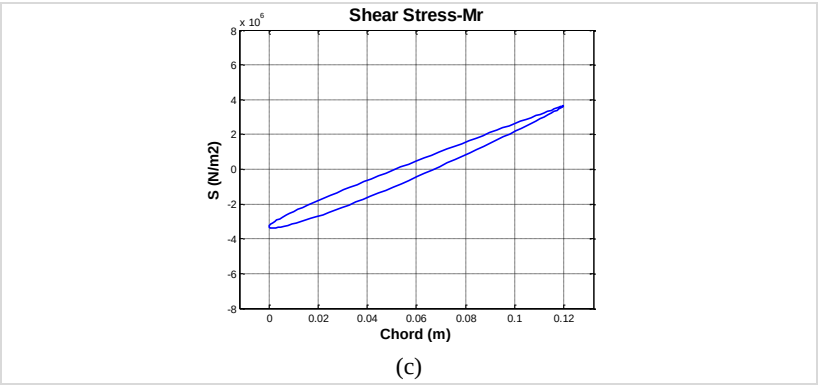

(c)

Figure 6.8 – NACA2412 airfoil in-plane stress for angle of attack α = 90°.

6.4 Concluding Remarks

This chapter has presented some stress results of the Shear Flow Theory for a blade cross-section subjected to unitary bending and torsional moments. The comparison of results obtained for a symmetric airfoil NACA0012 and for an asymmetric airfoil NACA2412 with the results calculated using the cross-sectional properties obtained by Wang et. al [18] has demonstrated the validity of this methodology for determining the in-plane stresses on thin-walled blades.

CHAPTER 7

CASE STUDY ON A LARGE WIND TURBINE

This chapter aims to apply the methodology presented in earlier chapters concerning thin-walled multilayer blades of large wind turbines on a work developed in the Energy Research Centre of the Netherlands (ECN) named "Upwind 20MW Wind Turbine Pre-Design", by Peeringa et al. [38]. From the design parameters of this work's large wind turbine, the blade geometry is generated and the aerodynamic loads are calculated. Then, the in-plane stresses are calculated for different stacking sequences of layers and the Tsai-Wu failure criterion is applied.

7.1 Design Parameters of the Large Wind Turbine

7.1.1 Basic Geometric Parameters

- Rotor Diameter: 252 m
- Hub Diameter: 6 m
- Maximum Chord c_{max}: 9.3 m

7.1.2 Basic Operational Parameters

- Wind speed U: 9.5 m/s
- Tip Speed Ratio λ: 8.5

7.1.3 Airfoil Distribution

- Between 87 - 126 m: NACA 64618
- Between 67 - 83 m: DU93-W-210
- Between 55 - 64 m: DU91-W2-250
- Between 43 - 52 m: DU97-W-300
- Between 37 - 43 m: DU00-W2-350
- Between 23 - 35.5 m: DU00-W2-401

- Between 13 - 22 m: Cylinder2
- Between 3 - 9 m: Cylinder

7.2 Stress Analysis on the Blade with Stacking Sequence #1

For the first stacking sequence, one defined a balanced and symmetric laminate with a thickness of 80 mm, composed of 16 layers considered to be 5 mm thick. The orientation of the fibers for each layer was defined as: 0º 90º 0º 90º 0º 90º 0º 90º | 90º 0º 90º 0º 90º 0º 90º 0º.

The next subsections present the results for the normal and shear stresses and Tsai-Wu on the three outermost layers: **0º 90º 0º** 90º 0º 90º 0º 90º | 90º 0º 90º 0º 90º 0º 90º 0º.

7.2.1 Stress distribution and the Failure Criterion on the Outermost Layer

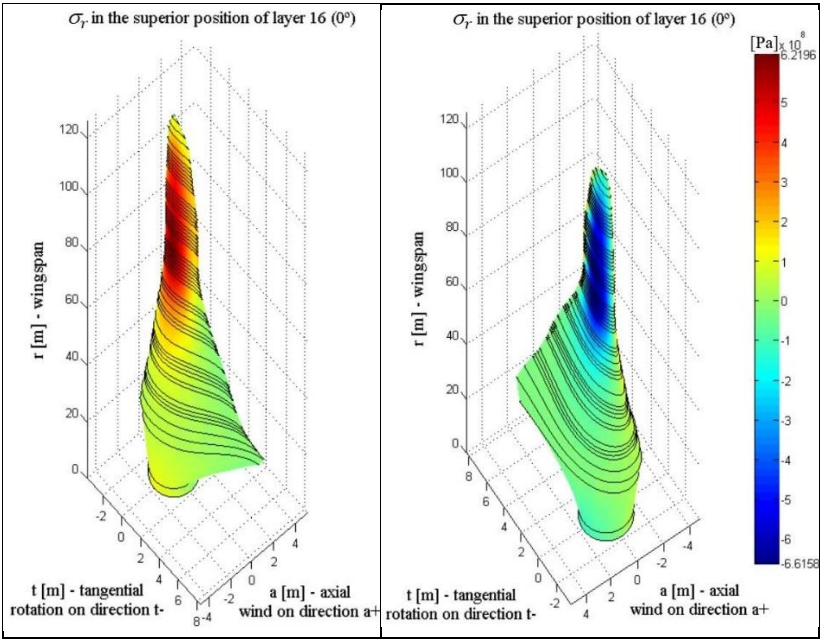

Figure 7.1 – Distribution of the normal stress σ_r in the superior position of layer 16, oriented at 0º.

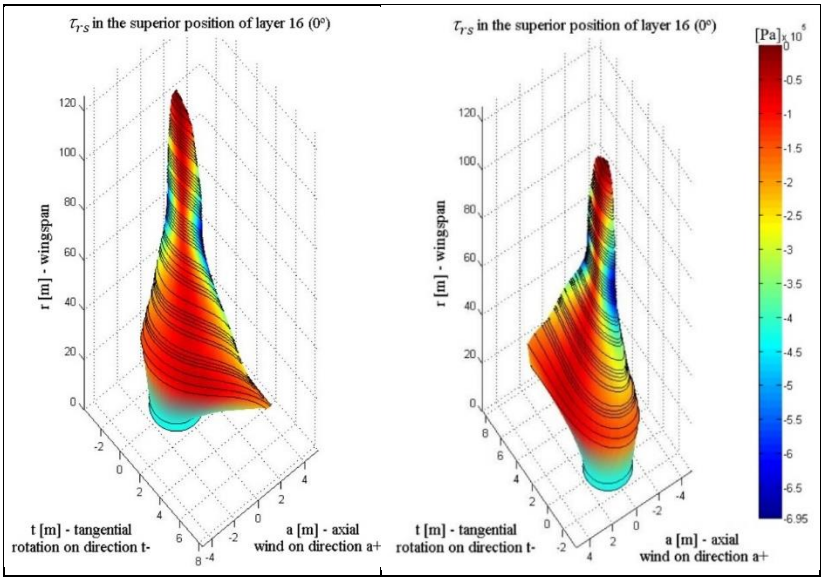

Figure 7.2 – Distribution of the shear stress τ_{rs} in the superior position of layer 16, oriented at 0°.

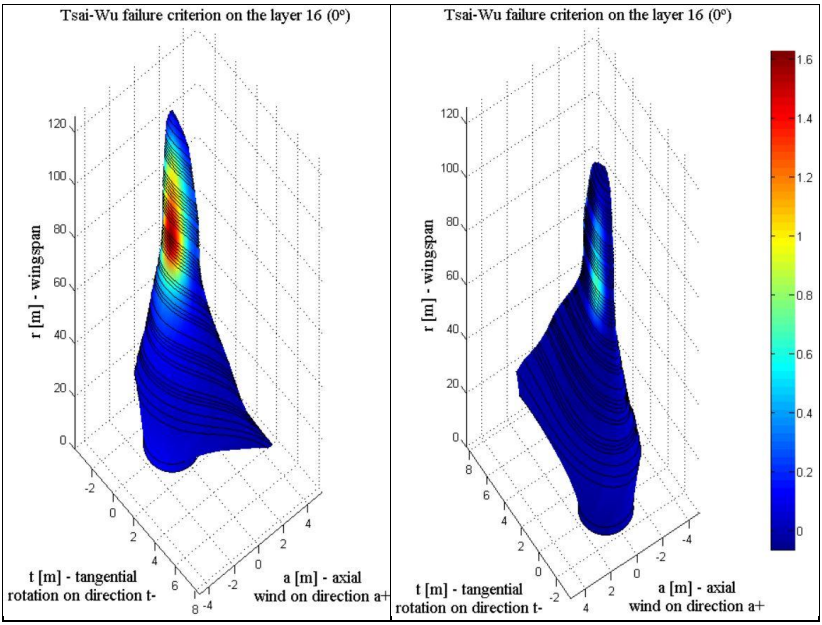

Figure 7.3 – Tsai-Wu failure criterion for the superior position of layer 16, oriented at 0º.

7.2.2 Stress distribution and the Failure Criterion on the Second Outermost Layer

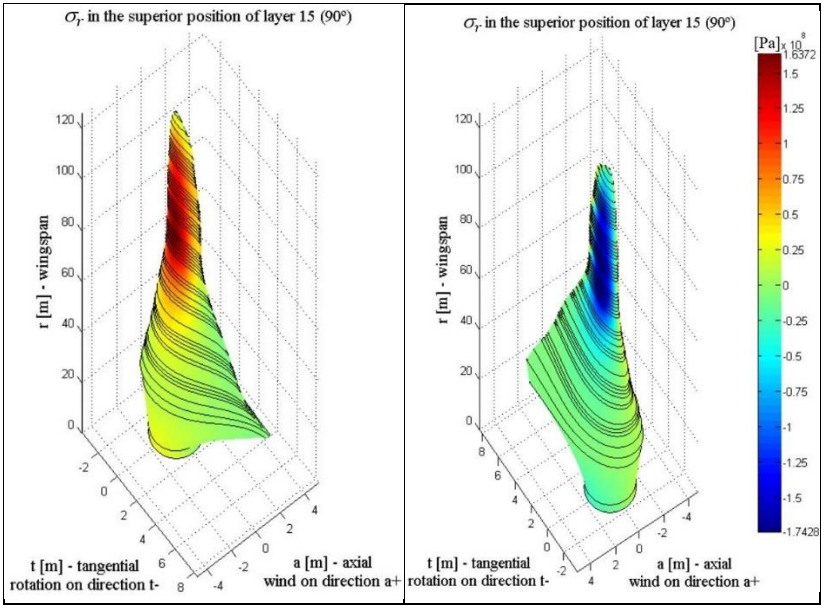

Figure 7.4 – Distribution of the normal stress σ_r in the superior position of layer 15, oriented at 90º.

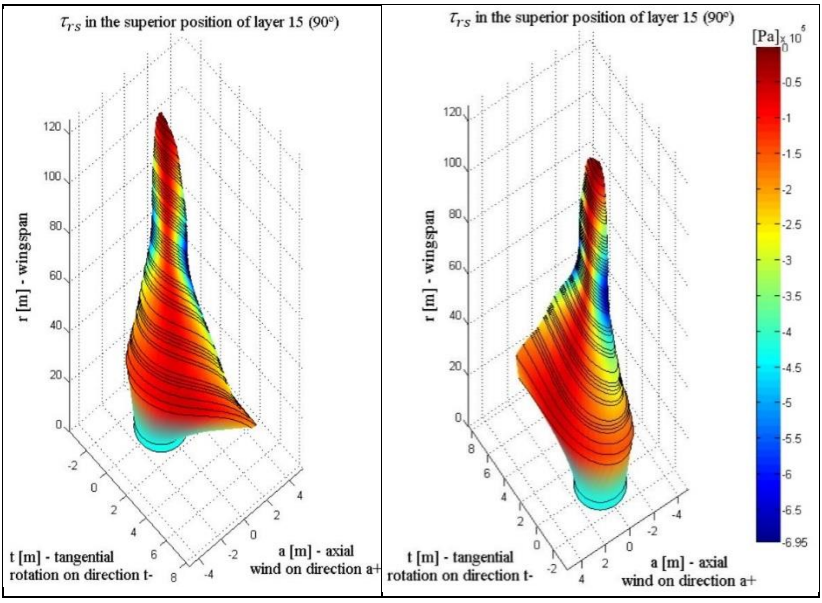

Figure 7.5 – Distribution of the shear stress τ_{rs} in the superior position of layer 15, oriented at 90°.

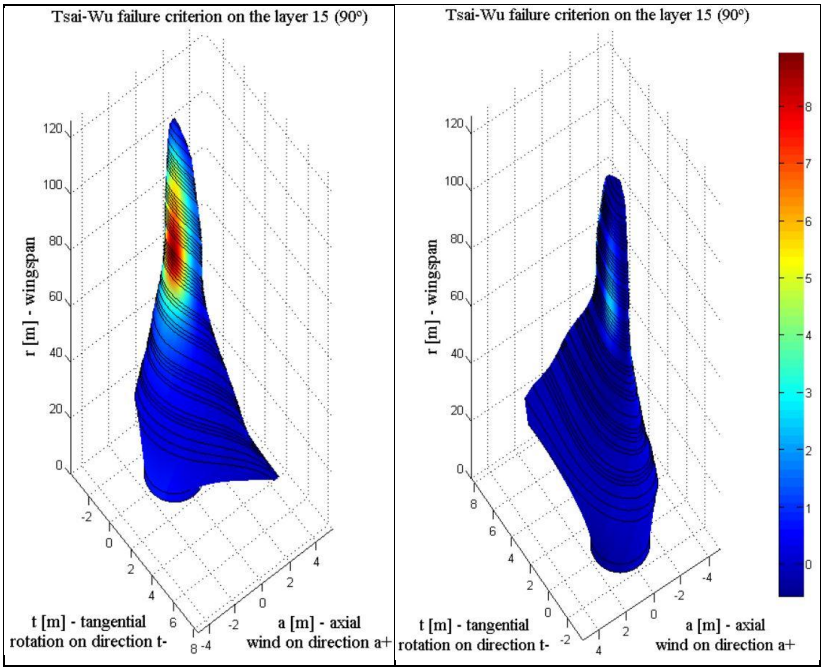

Figure 7.6 – Tsai-Wu failure criterion for the superior position of layer 15, oriented at 90º.

7.2.3 Stress distribution and the Failure Criterion on the Third Outermost Layer

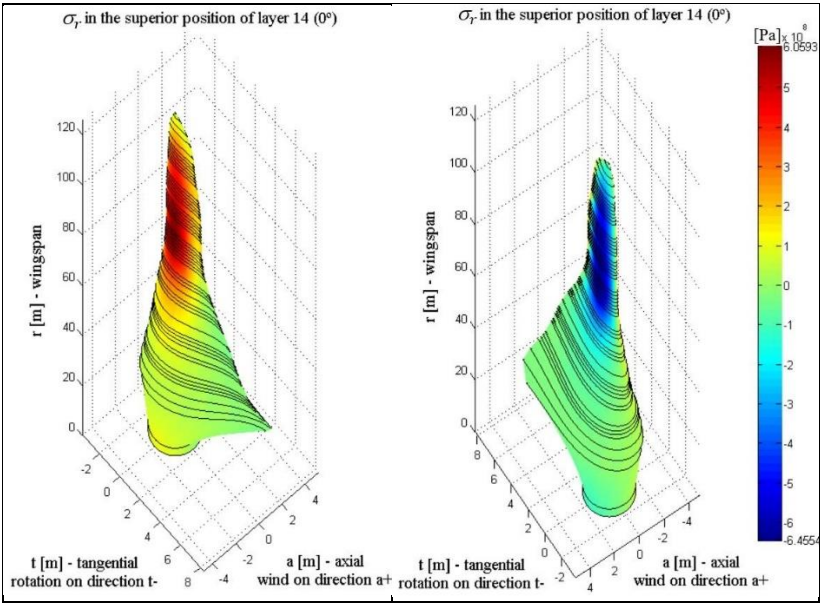

Figure 7.7 – Distribution of the normal stress σ_r in the superior position of layer 14, oriented at 0º.

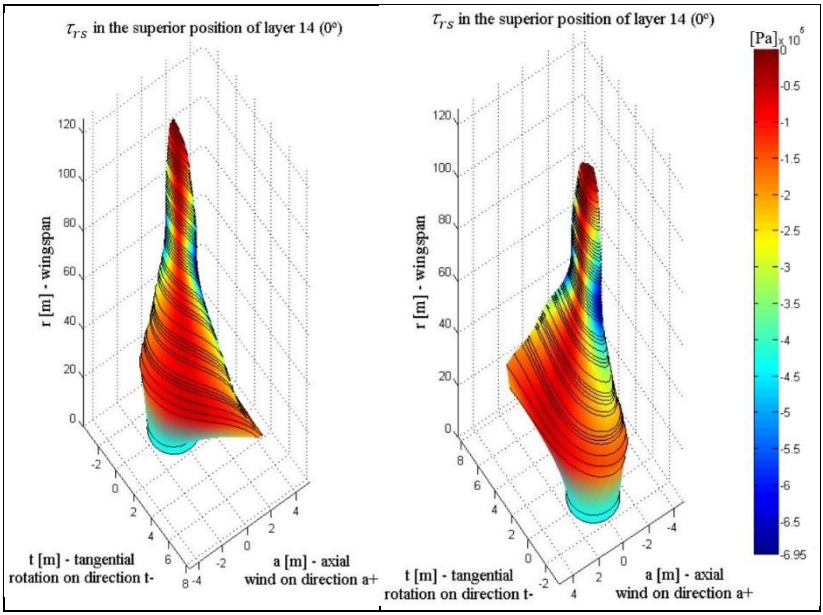

Figure 7.8 – Distribution of the shear stress τ_{rs} in the superior position of layer 14, oriented at 0º.

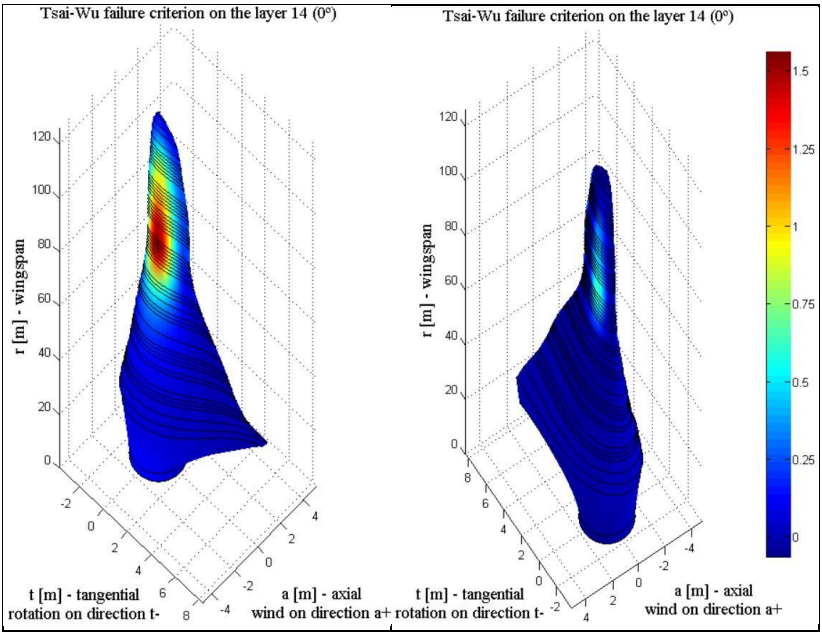

Figure 7.9 – Tsai-Wu failure criterion for the superior position of layer 14, oriented at 0º.

7.3 Stress Analysis on the Blade with Stacking Sequence #2

For the second stacking sequence, one defined a balanced and symmetric laminate with a thickness of 80 mm, composed of 16 layers considered to be 5 mm thick. The orientation of the fibers for each layer was defined as: 0º 45º -45 0º 0º 45º -45º 0º | 0º -45º 45º 0º 0º -45º 45º 0º.

The next subsections present the results for the normal and shear stresses and Tsai-Wu on the three outermost layers: **0º 45º -45** 0º 0º 45º -45º 0º | 0º -45º 45º 0º 0º -45º 45º 0º.

7.3.1 Stress distribution and the Failure Criterion on the Outermost Layer

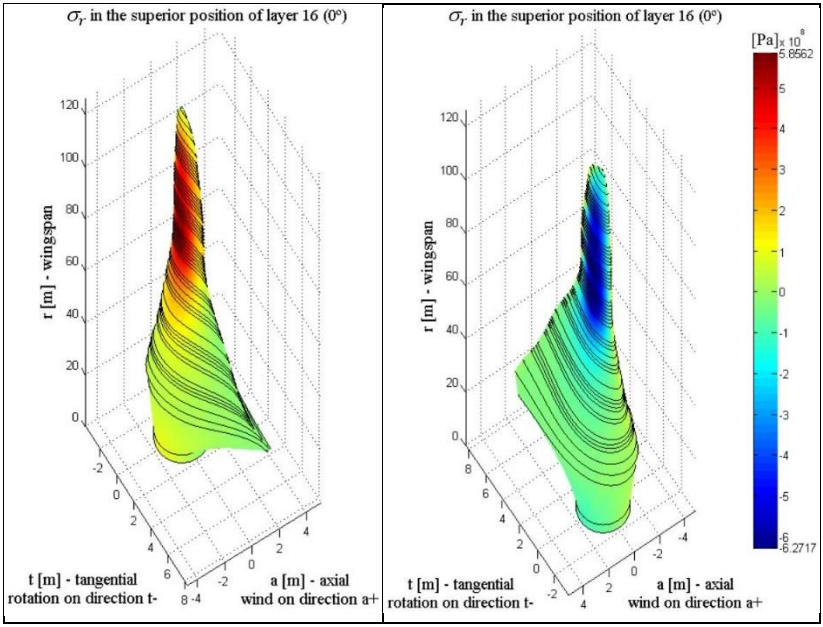

Figure 7.10 – Distribution of the normal stress σ_r in the superior position of layer 16, oriented at 0º.

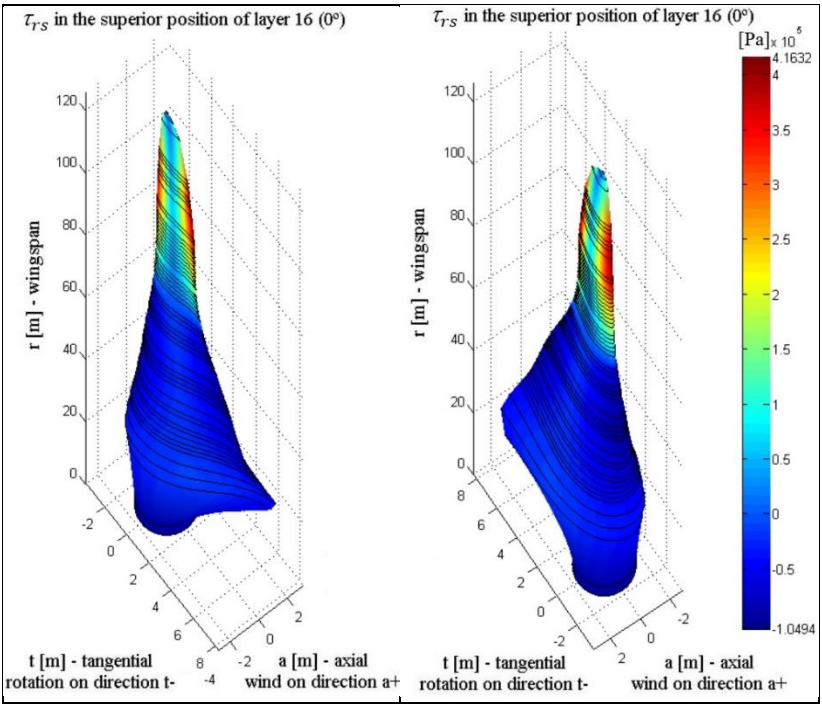

Figure 7.11 – Distribution of the shear stress τ_{rs} in the superior position of layer 16, oriented at 0º.

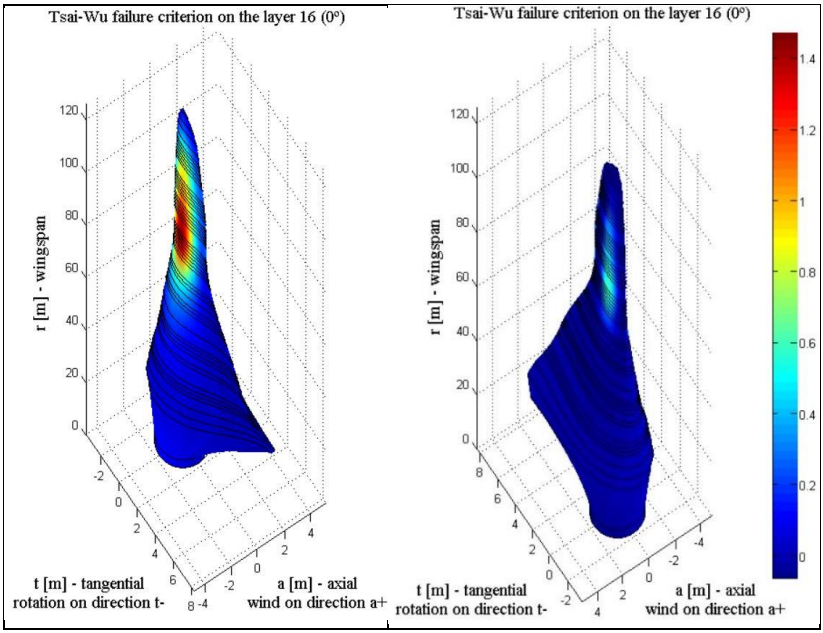

Figure 7.12 – Tsai-Wu failure criterion for the superior position of layer 16, oriented at 0º.

7.3.2 Stress distribution and the Failure Criterion on the Second Outermost Layer

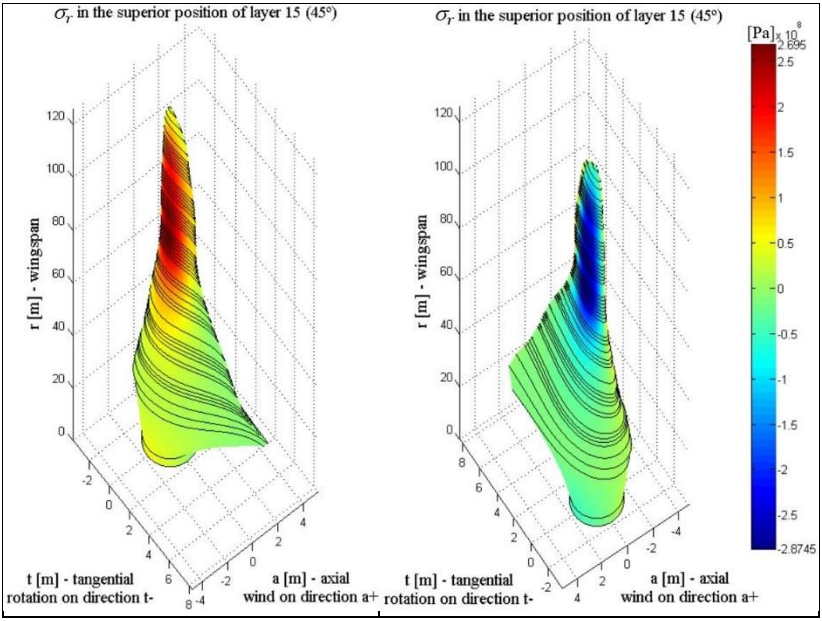

Figure 7.13 – Distribution of the normal stress σ_r in the superior position of layer 15, oriented at 45º.

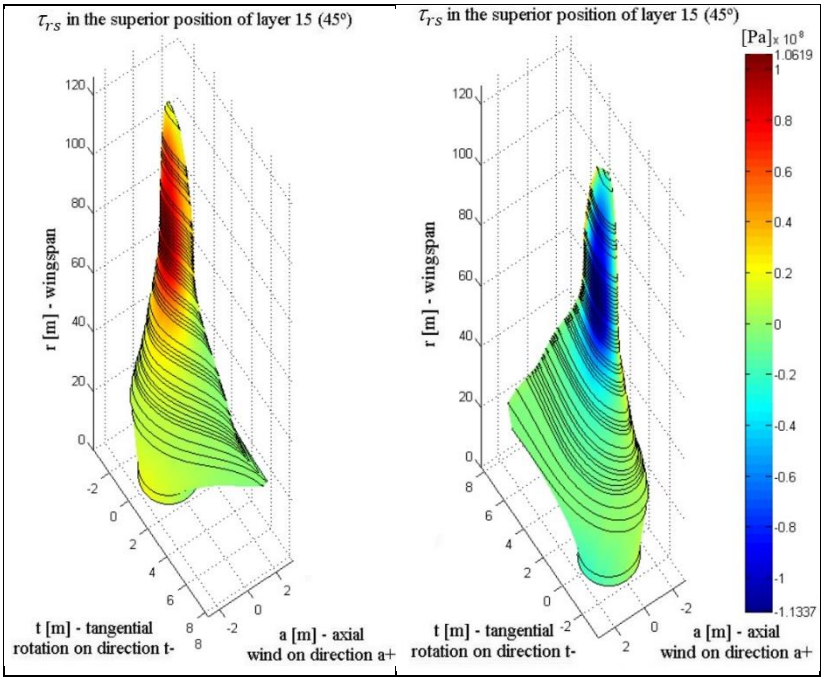

Figure 7.14 – Distribution of the shear stress τ_{rs} in the superior position of layer 15, oriented at 45º.

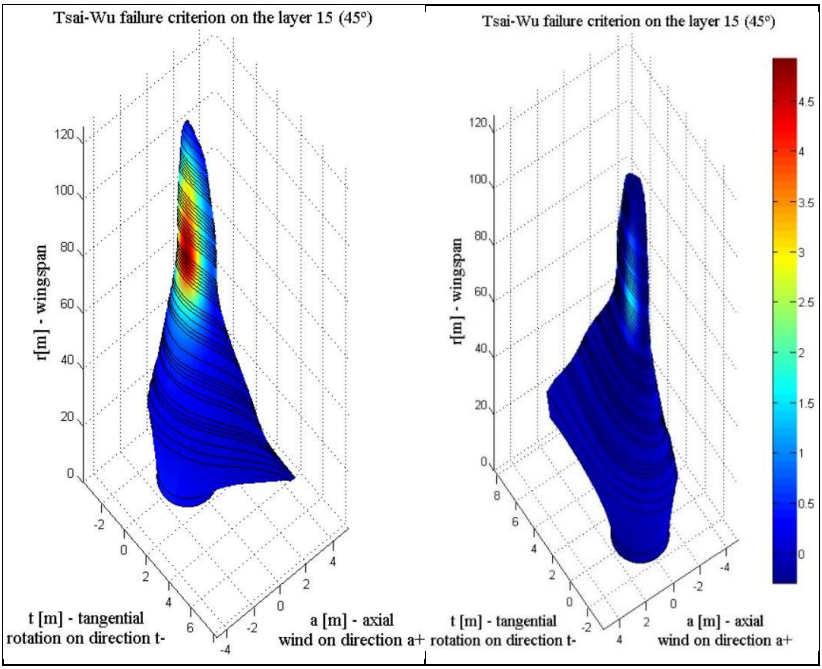

Figure 7.15 – Tsai-Wu failure criterion for the superior position of layer 15, oriented at 45º.

7.3.3 Stress distribution and the Failure Criterion on the Third Outermost Layer

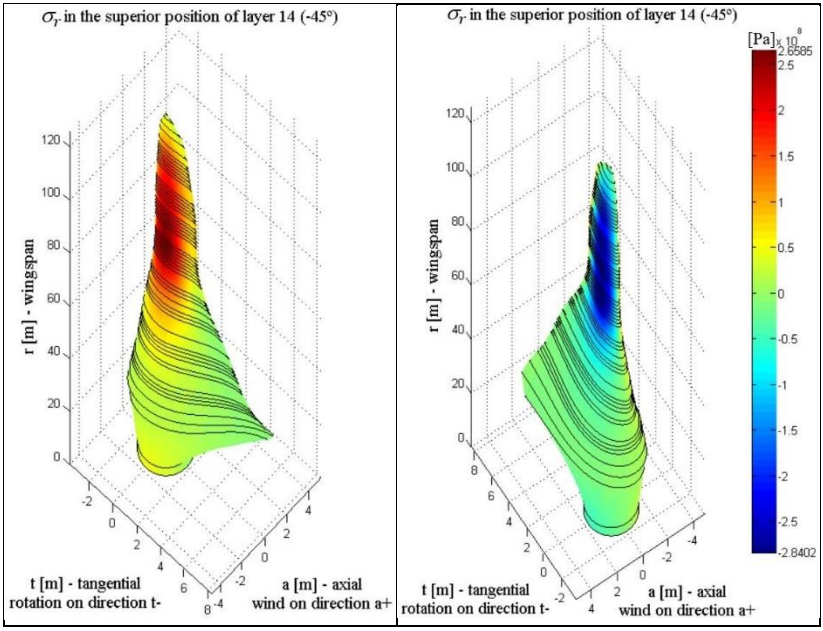

Figure 7.16 – Distribution of the normal stress σ_r in the superior position of layer 14, oriented at -45°.

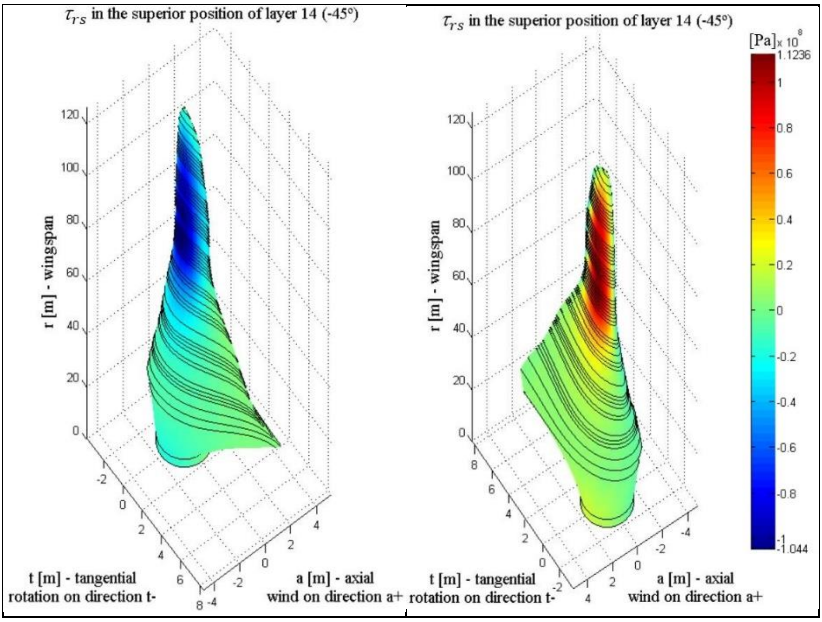

Figure 7.17 – Distribution of the shear stress τ_{rs} in the superior position of layer 14, oriented at -45º.

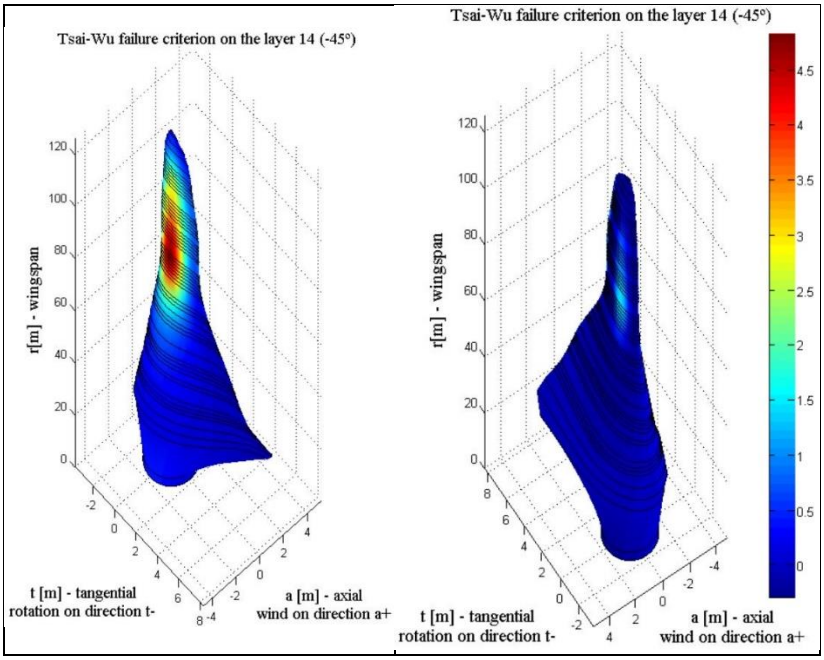

Figure 7.18 – Tsai-Wu failure criterion for the superior position of layer 14, oriented at -45º.

7.4 Concluding Remarks

In this chapter, a stress analysis has been performed on thin-walled multilayer blades on a hypothetical 20 MW wind turbine designed in the Energy Research Centre of the Netherlands (ECN) [38]. Two different stacking sequences of layers were evaluated and the in-plane stress distribution and the Tsai-Wu failure criterion were shown for the three outermost layers. The blade with the second stacking sequence (0º 45º -45 0º 0º 45º -45º 0º | 0º -45º 45º 0º 0º -45º 45º 0º) has shown to be slightly stronger than the first one (0º 90º 0º 90º 0º 90º 0º 90º | 90º 0º 90º 0º 90º 0º 90º 0º), since the torsional moments on the turbine blades were not neglected. The stress analyses have shown consistency and coherence,

since the results for the normal stresses σ_r show the upper surface of the blade under compression and the lower surface under tension, since the highest stresses appear in the slenderer outermost part of the blade, where the aerodynamic efficiency is usually prioritized for being where most of the energy is extracted from the wind. This stress analysis can be used to optimize the material usage and the layers orientation during the construction process of the blade. It is also worth noting that, when adding centrifugal and gravitational loads to the blades, they will be proportionally more stressed in the radial direction, what would require more layers at 0^o.

CHAPTER 8

CONCLUSIONS

This chapter summarizes the research work carried out for this dissertation and lays some recommendations and scope for future research concerning the study and design of large wind turbines.

8.1 Summary

From this dissertation, one was able to learn about the latest advances and trends in wind turbine technology, such as the trend of the specific powers lowering and the expansion of the turbines rotors. It was seen that the construction, transportation, installation and operation of large wind turbines developed for energy production at sites with lower wind speeds demand the overcoming of many challenges regarding the turbine technology, particularly the blades, such as the fact that, by increasing the length of the blades, the gravitational loads increase at a cubic rate against a quadratic increase of the power extracted. These challenges require materials science innovations, aerodynamic and structural design optimization and also more accurate and efficient computational models. For the aerodynamic model, for example, one way to enhance it is to more precisely determine the Reynolds number through an iterative process, since experimental data for such high Reynolds are scarce.

The models also must predict the bending and torsional moments acting on the blade span accurately for the preliminary stress analysis evaluation. For the in-plane normal and shear stresses calculation, the methodology presented has proved to be simple to implement and coherent in the results obtained, being aware of its limitations.

About those, it must be addressed here that the results were obtained only for the blade shells and also that large deformations were not considered, which does not represent the reality, since, mainly without an internal structure of spar and fillings, the blade would suffer large deformations.

Thereafter, the resulting warping of the blade cross-section should be considered by using higher order shell theories in order to achieve more reliable results.

Finally, through the application of fiber-reinforced plastic materials, one can obtain a higher strength/weight ratio in order to mitigate the issues related to the expansion of the blades lengths. Also, one can vary the orientation of the fibers and the stacking sequence of the layers in a multilayer configuration in order to increase the laminate strength.

8.2 Scope for Future Works

Possible and desirable extensions of the work carried out in this dissertation are:

- The variation of the number of layers, i.e. laminate thickness, along the wing span for an optimal material usage and structural efficiency;
- The inclusion of centrifugal, gravitational and gyroscopic loads;
- The modeling of the internal structure, e.g. shear webs, in the cross-section of the blade in order to better adequate its stiffness to reality and introduce the calculation of the transverse shear stresses on the shear webs;
- Verification of the results by the integration of the computational fluid dynamics and the structural analysis.

REFERENCES

[1] Sathyajith, M. *"Wind Energy – Fundamentals, Resource Analysis and Economics"*. Springer, India, 2006.

[2] Burton, T. et al. *"Wind Energy Handbook"*. 2nd edition, John Wiley & Sons Ltd. England, 2011.

[3] U.S. Department of Energy, NREL - National Renewable Energy Laboratory, SRA International Inc., New West Technologies. "*Enabling Wind Power Nationwide*". Report. May 2015.

[4] Griffith, D; Ashwill, T. *"The Sandia 100-meter All-glass Baseline Wind Turbine Blade: SNL100-00"*. Sandia Report. Sandia National Laboratories, 2011.

[5] http://www2.aneel.gov.br/aplicacoes/atlas/pdf/06-energia_eolica(3).pdf, accessed in 07/2016.

[6] Wiser, R. et al. *"2013 Wind Technologies Market Report"*. DOE/GO-102014-4459. Washington, DC: U.S. Department of Energy, Office of Energy Efficiency & Renewable Energy, August 2014.

[7] http://www.renewableenergyworld.com/rea/news/article/2014/02/meet-the-new-worlds-biggest-wind-turbine, accessed in 02/2015.

[8] http://www.windpowermonthly.com/10-biggest-turbines, accessed in 02/2015.

[9] http://keystonetowersystems.com/in-field/, accessed in 08/2016.

[10] CEMAC – Clean Energy Manufacturing Analysis Center. *"CEMAC 2015 Research Highlights"*. U.S. Department of Energy, March 2016.

[11] http://energy.gov/eere/next-generation-wind-technology, accessed in 03/2015.

[12] Li, L. et al. *"A Mathematical Model for Horizontal Axis Wind Turbine Blades"*. School of Mechanics and Engineering, Southwest Jiaotong University, Chengdu 610031 and Department of Mathematics, Kunming University, Kunming 650214 China. Elsevier Science Ltd, 2013.

[13] Chopra, I.; Dugundji, J. *"Non-linear Dynamic Response of a Wind Turbine Blade"*. Journal of Sound and Vibration, Department of Aeronautics and Astronautics, Massachusetts Institute of Technology, Cambridge, Massachusetts 02139, USA, 1979.

[14] Lee, D.; Hodges, D. H.; Patil, M. J. *"Multi-flexible-body Dynamic Analysis of Horizontal Axis Wind Turbines"*. School of Aerospace Engineering, Georgia Institute of Technology, Atlanta, Georgia, USA. John Wiley & Sons Ltd, 2002.

[15] Baumgart, A. *"A Mathematical Model for Wind Turbine Blades"*. Forskningscenter Risø, Prøvestationen for Vindmøller, Roskilde, Denmark. Elsevier Science Ltd, 2002.

[16] Kallesøe, B. S. *"Equations of motion for a rotor blade, including gravity, pitch action and rotor speed variations"*. Department of Mechanical Engineering, Technical University of Denmark, Lyngby, Denmark. John Wiley & Sons Ltd, 2007.

[17] Ramakrishnan, V.; Feeny, B. F. *"In-plane nonlinear dynamics of wind turbine blades"*. Proceedings of the ASME 2011 International Design Engineering Technical Conferences & Computers and Information in Engineering Conference, Washington, DC, USA, August 28–31, 2011.

[18] Wang, L. et al. *"A mathematical model for calculating cross-sectional properties of modern wind turbine composite blades"*. School of Computing, Engineering and Physical Sciences, University of Central Lancashire, Preston, UK; Sustainable Engineering, University of Cumbria, Energus, Workington, UK; State Key Laboratory of Solidification Processing, Northwestern Polytechnical University (NWPU), Xi'an, PR China. Elsevier Science Ltd, 2013.

[19] Pilkey, W. D. *"Analysis and Design of Elastic Beams"*. Wiley Online Library, 2002.

[20] Capuzzi, M.; Pirrera, A.; Weaver, P. M. *"A Novel Adaptive Blade Concept for Large-Scale Wind Turbines. Part I: Aeroelastic behaviour"*. Advanced Composites Centre for Innovation and Science, Aerospace Engineering Department, University of Bristol, Bristol, UK. Elsevier Ltd, 2014.

[21] Capuzzi, M.; Pirrera, A.; Weaver, P. M. *"A Novel Adaptive Blade Concept for Large-Scale Wind Turbines. Part II: Structural Design and Power Performance"*. Advanced Composites Centre for Innovation and Science, Aerospace Engineering Department, University of Bristol, Bristol, UK. Elsevier Ltd, 2014.

[22] http://www.power-eng.com/articles/print/volume-118/issue-3/features/advancements-in-wind-turbine-technology-improving-efficiency-and-reducing-cost.html, accessed in 04/2016.

[23] http://www.renewablesinternational.net/a-silent-revolution-in-the-wind-sector/150/435/87652/, accessed in 04/2016.

[24] http://alstomenergy.gepower.com/fr/products-services/product-catalogue/production-electricite/energies-renouvelables/eolien/eoliennes-offshore/plateforme-eoliennes-offshore-haliade/index.html, accessed in 08/2016.

[25] http://cleantechnica.com/2015/09/16/texas-set-wind-turbine-leader-nuts-bolts/, accessed in 05/2016.

[26] http://www.compositesworld.com/articles/modular-design-eases-big-wind-blade-build, accessed in 05/2016.

[27] http://cleantechnica.com/2016/01/29/mammoth-50-mw-wind-turbine-blades-revolutionise-offshore-wind-us/ , accessed in 05/2016.

[28] https://share.sandia.gov/news/resources/news_releases/big_blades/#.V6veoSgrJhF accessed in 05/2016.

[29] Loth, E.; Steele, A.; Ichter, B. *"Segmented Ultralight Pre-Aligned Rotor for Extreme-Scale Wind Turbines"*. American Institute of Aeronautics and Astronautics, 2012.

[30] Manwell, J. F.; McGowan, J. G.; Rogers, A. L. — *"Wind Energy Explained: Theory, Design and Application"*. University of Massachusetts, Amherst, US. John Wiley & Sons, 2002.

[31] Loureiro, D. *"Relatório de Atividades de Estágio – Turbinas Eólicas de Eixo Horizontal de Grande Porte"*. Internal Report. Grante, Department of Mechanical Engineering, Federal University of Santa Catarina, Florianópolis, Brazil, 2014.

[32] Hau, E. *"Wind Turbines: Fundamentals, Technologies, Application, Economics"*. 2nd edition, Springer. Germany, 2006.

[33] http://www.renewableenergyworld.com/articles/2014/04/advancements-in-wind-turbine-technology-improving-efficiency-and-reducing-cost.html, accessed in 12/2014.

[34] Ceyhan, O. *"Towards 20 MW Wind Turbine: High Reynolds Number Effects on Rotor Design"*. Presented at the 50th AIAA ASM Conference, 9-12 January 2012, Nashville, Tennessee, USA, 2012.

[35] Drela, M. and Youngren, H. (2011) XFOIL 6.9 User Primer, URL http://web.mit.edu/drela/Public/web/xfoil/

[36] Reddy, J. N. *"Theory and Analysis of Elastic Plates and Shells"* 2nd Edition, CRC Press, Taylor & Francis Group, 2007.

[37] Whitney, J. M.; Daniel, I. M.; Pipes, R. B. *"Experimental Mechanics of Fiber Reinforced Composite Materials"*. The Society for Experimental Mechanics, 1984.

[38] Peeringa, J.; Brood, R.; Ceyhan, O.; Engels, W.; De Winkel, G. *"Upwind 20MW Wind Turbine Pre-Design – Blade design and control"*. Energy Research Centre of the Netherlands (ECN), December 2011.